

Semi-confined supernova feedback in HII region bubbles

Cheryl S. C. Lau¹* and Ian A. Bonnell¹

¹*School of Physics and Astronomy, University of St Andrews, St Andrews KY16 9SS, UK*

Accepted XXX. Received YYY; in original form ZZZ

ABSTRACT

Galactic-scale simulations rely on sub-grid models to provide prescriptions for the coupling between supernova (SN) feedback and the interstellar medium (ISM). Many of these models are computed in 1-D to allow for an efficient way to account for the variability of properties of their local environment. However, small-scale simulations revealed that the release of energy from SNe within molecular clouds can be highly asymmetrical. This is largely due to the presence of pre-SN feedback, such as ionizing radiation, that are able to carve cavities and channels around the progenitors prior to their detonation. Being partially confined, the SN energy escapes into the outer ISM preferentially through these channels, departing from the spherically symmetric 1-D descriptions. To understand by how much the feedback output could differ, we present a theoretical model for a semi-confined SN. The problem concerns a SN expanding into an evolved HII region, bounded by a molecular cloud with pre-existing vents. With the aid of simple 3-D hydrodynamical simulations, we show that this mode of energy release increases the local dynamical impact of the outflows, and extends the timescales over which the SN is energetically coupled to the surrounding matter. We also show that the amount of small-scale solenoidal turbulence driven by semi-confined SNe may be amplified.

Key words: ISM: supernova remnants – ISM: bubbles – methods: analytical – methods: numerical

1 INTRODUCTION

From the scales of molecular clouds up to galaxies, it is generally recognized that supernova (SN) feedback is one of the key mechanisms for regulating star formation (e.g. Larson 1974; Hopkins et al. 2011; Körtgen et al. 2016). The energy imparted on to the interstellar medium (ISM) from Type II SNe, on Galactic average, dominates over the contributions from ionizing radiation and stellar winds over the lifetime of the OB-type stars (Mac Low & Klessen 2004). SNe are also largely responsible for cosmic ray acceleration (e.g. Pfrommer et al. 2017), chemical enrichment of the ISM (e.g. Goswami et al. 2021), and the replenishing of supersonic turbulence in molecular clouds (e.g. Joungh & Mac Low 2006; Hennebelle & Iffrig 2014). SN explosions from multiple massive stars can collectively form superbubbles that drive the galactic fountains (e.g. Keller et al. 2015; Kim et al. 2016), and play a fundamental role in determining the star formation efficiencies across all scales (e.g. Ostriker & Shetty 2011). It is therefore inevitable to investigate the energy and momentum deposition from SNe on its local environment in order to understand how these ecosystems operate.

Quantifying the coupling efficiency between SNe and their immediate surroundings remains a challenge. For one, SN shocks are subjected to radiative cooling. Depending on the density structure of the molecular cloud, a significant portion of the injected thermal energy could be radiated away before making any substantial dynamical impact on the cold ISM (e.g. McKee & Ostriker 1977; Cowie et al. 1981; Walch & Naab 2015). For two, which is often deemed the primary reason, is that the evolution of SN remnant is heavily influenced by the pre-SN stellar feedback (e.g. Borkowski et al. 1996;

Dwarkadas 2005; Rogers & Pittard 2014; Lucas et al. 2020). This feedback could originate from the SN progenitor star itself during its earlier phases, or from the neighbouring massive stars in the OB association (Oey & Clarke 1997). Either way, SN remnants likely expand into a circumstellar environment that has been modified.

Ionizing radiation, for example, are shown to be able to create cavities and bubbles of around 10 pc in radius inside molecular clouds (e.g. Dale et al. 2013, 2014; Fichtner et al. 2024). The Lyman continuum radiation from massive stars ionizes the surrounding gas up to the Strömgren radius (Strömgren 1939) and heats them to approximately 10^4 K with the excess energy (Osterbrock 1974). Upon reaching ionization equilibrium, the HII region begins to expand under thermal overpressure (D-type expansion; Spitzer 1978). Because the ionization front is supersonic to the neutral ambient medium, a dense shell of shocked neutral gas is formed, sweeping across the ISM as the HII region evolves (e.g. Hosokawa & Inutsuka 2006; Raga et al. 2012; Bisbas et al. 2015).

Similarly, stellar winds from Wolf-Rayet stars with terminal velocities up to 3000 km s^{-1} are also capable of driving a circumstellar shell of shock-heated gas (e.g. Castor et al. 1975; Weaver et al. 1977; Geen & de Koter 2022). This also applies to the massive runaway stars that have migrated (Haid et al. 2018; Meyer 2024). Indeed, stars that pass frequently through the dense regions are likely unable to develop wind-blown bubbles, given that they may also be inhibited by the large-scale accretion flows (Dale & Bonnell 2008). Yet, a later study by Mackey et al. (2014) proposed that static shells may still be formed around a runaway progenitor if the cavity is subjected to external ionizing radiation. This illustrates the necessity to consider SN shock collisions with the surrounding swept-up matter (Dwarkadas 2005; Walch & Naab 2015), whilst also accounting for the non-linear

* E-mail: csc11@st-andrews.ac.uk (CSCL)

interplay between the winds and the ionizing radiation (e.g. Freyer et al. 2006; Haid et al. 2018; Geen et al. 2023).

However, galactic-scale simulations are often unable to resolve down to parsec or sub-parsec scales where these feedback interactions take place. The lack of resolution may also provoke numerical overcooling (e.g. Katz 1992; Springel & Hernquist 2002; Creasey et al. 2011; Dalla Vecchia & Schaye 2012) where radiative losses are erroneously amplified. For this reason they rely on sub-grid models, that serve as prescriptions of the feedback’s overall impact (e.g. Thacker & Couchman 2000; Stinson et al. 2006; Oku et al. 2022). The use of sub-grid models addresses the spurious cooling and allows for a more accurate estimate of the energy deposition. Nonetheless, the precise injection method and the SN energy budget can introduce large uncertainties to the galactic evolutionary models (e.g. Rosdahl et al. 2017; Keller & Kruijssen 2022). Refining these feedback prescriptions has thus been a priority in numerical development, and the results from cloud-scale simulations of SNe (e.g. Körtgen et al. 2016) provide this crucial missing piece of puzzle.

To study the local energy deposition from SN, recently there has also been a growing tendency to employ 1-D hydrodynamic models. Their low computational costs enable large parameter grids to be scanned to account for a variety of complex ISM environments, such as different density distributions or turbulent structures (Haid et al. 2016). It may also account for different evolutionary phases of the feedback bubble from varying star formation efficiencies (Rahner et al. 2017). These models can further cover a range of SN progenitors by adopting stellar models, which allow the ejecta energy to be self-consistently computed from the stellar core properties (Fichtner et al. 2022; Fichtner et al. 2024).

An issue with 1-D models, however, is that they are bound to model the SN output in a spherically symmetric manner¹. Previous studies by Rogers & Pittard (2014); Wareing et al. (2016, 2017); Lucas et al. (2020) unanimously suggested that this is often not the case. The pre-SN feedback, including ionizing radiation and stellar winds, are able to follow the paths of least resistance within the molecular cloud where gas densities are relatively low. These *channels* serve as chimneys that connect the embedded feedback-driven cavities towards the outer ISM. The energy from the first SN, which detonates a few Myr after the onset of feedback, would preferentially leave the cloud through the pre-existing channels, leaving a minimal impact on the dense structures (Lucas et al. 2020). As such, the outflows from SNe exploding within feedback-driven bubbles are likely highly anisotropic.

In fact, this mode of SN energy release has been long theorized by Morfill & Tenorio-Tagle (1983); Falle & Garlick (1982); Tenorio-Tagle et al. (1985), who applied 2-D hydrodynamical calculations to model the SN energy outbreaks from embedded progenitors near the edge of molecular clouds (see also HII region *champagne flows*). These models were proposed to explain the the complex velocity profile of the Cygnus Loop. The large asymmetry in its blowouts led to the conjecture that its peculiar morphology is caused by SN shocks encountering the inner walls of a wind-blown bubble, with breakouts through the shell into lower density ISM (Aschenbach & Leahy 1999; Uchida et al. 2008). Various alternative interpretations have been proposed (e.g. Meyer et al. 2015; Fang et al. 2016) but

¹ For 1-D models, statistical methods may be applied to account for any directional variations (e.g. Haid et al. 2016, for densities in turbulent medium), or through parametrization (e.g. Harper-Clark & Murray 2009; Rahner et al. 2017, for shell cover fractions), but it would still require results from 3-D simulations to formulate these compensation methods.

nevertheless support the idea that a SN remnant evolving within a pre-existing non-spherical cavity shaped by its progenitor is responsible for the observed mixed-velocity emissions (see also e.g. Borkowski et al. 2017).

The question here is: by how much would the energy and momentum deposition differ if the SNe were subjected to partial confinement? In another words, to what extent do 1-D sub-grid models hold given that SN outflows are likely expelled in preferential directions? Past studies that investigated on the porosity of feedback bubbles typically place their focus on the *loss* of kinetic energy (Rosen et al. 2014), momentum flux (Dale & Bonnell 2008) or HII gas pressure (Harper-Clark & Murray 2009; Lopez et al. 2011, 2014) in order to explain the inconsistencies between the feedback energy input and the observed low X-ray emission luminosities. Less attention was given to their *positive* impacts. Geen et al. (2023), for example, suggested that the plumes formed by wind bubbles that break out from thin chimneys can lead to faster expansion velocities, and drive stronger fluid eddies at where the plume interacts with the ISM. This motivates our paper, to investigate what physical properties of the feedback outflows are *enhanced* due to the semi-confinement.

This paper is organized as follows. In Section 2, we present our novel analytical model of a partially confined SN. In Section 3, we describe the numerical methods to test these theoretical models with 3-D hydrodynamical simulations. Section 4 presents the results examining the outflows, the energy deposition, and the driven turbulence from semi-confined SNe. Finally, we summarize in Section 5.

2 THEORETICAL MODEL

We first tackle our problem via an analytic approach to model how SN energy escapes the feedback bubbles. In the present study, we focus on HII regions driven by photoionization, since their interior properties are relatively more uniform and hence allow for simpler approximations. Extensions to treat wind-blown bubbles or a combination of both would be ideal in future work.

The aim is to quantify the difference in outflows and energy output between a 1-D SN model and one which considers the confinement effect. To this end, we consider two models: (a) a *free-field SN*, that is, a spherical blast in a uniform medium, and (b) a *semi-confined SN*, whereby the blast detonates within a feedback-driven bubble. Such comparisons provide insights on how much 1-D sub-grid models would underpredict or overpredict the actual amount of feedback. The problem in concern is depicted in Fig. 1.

On the left, a free-field SN model is shown. The uniform medium in this scenario can represent, either, the ambient ISM, or a “smeared” molecular cloud that resembles a sub-grid model. On the right, our semi-confined model is presented. We consider a progenitor surrounded by an evolved HII region, bordered by a swept-up shell of dense gas. The HII region here acts as a representative of the feedback-driven cavities formed within molecular clouds. We also consider a low-density warm envelope around the molecular cloud that serves as the external medium (e.g. Wannier et al. 1983; Lucas et al. 2017). This envelope represents the outer parts of the cloud that are exposed to external FUV radiation fields and are predominantly formed of atomic gas due to the lack of shielding. Its warm temperature exerts a slight thermal pressure that keeps the cloud super-virial and less likely to be completely dispersed by feedback (Dale et al. 2012). In reality, the transition from atomic gas to molecular in the photodissociation regions should be gradual, as the level of shielding required by H₂ and CO differ (Wolfire et al. 2010), but following Lucas et al. (2017) we assert that this simplified geometry is sufficient

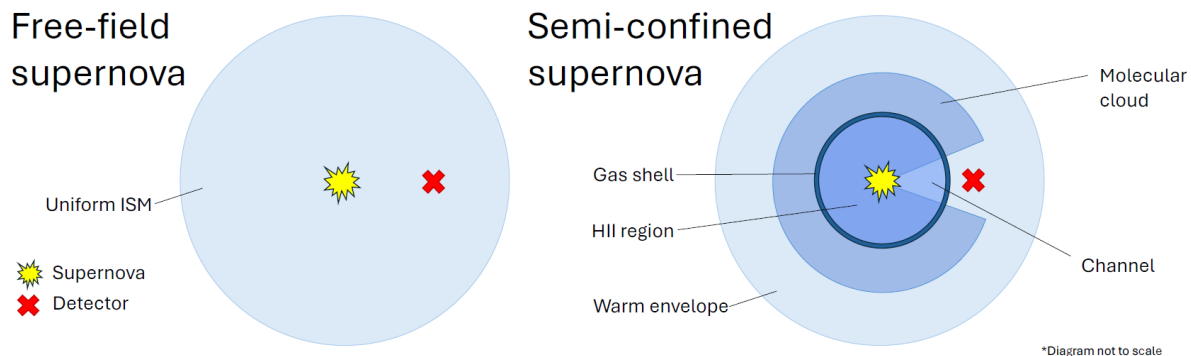


Figure 1. *Left:* Illustration of a free-field SN model. The SN detonates within a uniform medium, and a detector (marked by a cross) is placed at some distance away from the progenitor to measure the gas properties (see Section 4.3). *Right:* Illustration of a semi-confined SN model. The progenitor is embedded inside an HII region bordered by a dense shell of swept-up gas, surrounded by a molecular cloud. The cloud is enveloped by warm diffuse gas that represents the outer ISM environment. The HII region and the warm envelope are connected by a low-density channel. A detector is placed at the channel opening to measure the strength of the outflow (see Section 4.3).

to serve the purpose. Crucially, there is a low-density channel that connects the cavity to this envelope.

There are a few reasons for using models with simple geometries as a first proof of concept. First, it amplifies the effect of semi-confinement, allowing easier identification. Secondly, it removes the stochastic influence from density structures developed from turbulence, allowing for a higher degree of control over the amount of venting that the SN remnant experiences. This is similar to varying the fractal dimension of the cloud (Walch et al. 2012), but with well-defined holes that enable the rate of mass loss to be precisely calculated. Finally, it serves as a testing ground for understanding the physics behind SN energy release via channels. These findings may be then applied to turbulent cloud simulations to determine whether or not the semi-confinement effects are at play.

2.1 Semi-confined supernova

The release of SN energy from cavities is analogous to the problem of vented explosions in engineering, which concerns detonations within partially confined environments such as rooms fitted with windows. We conjecture that their theoretical descriptions are self-similar and may be applied to astrophysics. As such, we developed our semi-confined SN model based on the work of Feldgun et al. (2011, 2016), who studied the gas outflows and residual pressure relief from the vents of confined volumes after interior explosions. Our way to quantify the strength of the outflow is to consider a ‘detector’ placed at the opening of the channel (see Fig. 1). The following calculations model the time-evolution of gas velocity and pressure at the location of this detector. Note that the precise values for the physical parameters involved in the equations will be given in Section 4.1.1 and Section 4.1.2.

2.1.1 Initial conditions

The semi-confined scenario depicted in Fig. 1 sets from the time shortly after the first SN. The HII region is assumed to have reached its stagnation radius r_{HII} during the end phase of D-type expansion. Suppose the current HII region has volume V_{HII} and density ρ_{HII} . Given that its temperature T_{HII} is typically at around 10^4 K, we can

compute the cavity’s specific internal energy u_{HII} via the relation

$$u = \frac{kT}{\mu m_H (\gamma - 1)}, \quad (1)$$

where k is the Boltzmann constant, μ is the mean molecular weight, m_H is the hydrogen mass, and $\gamma = C_P/C_V = 5/3$ for ideal monatomic gas. From this, we obtain its gas pressure p_{HII} using the adiabatic equation of state,

$$p = \rho (\gamma - 1) u. \quad (2)$$

Hence, all of our calculations rely on an adiabatic assumption. The effects of radiative cooling are accessed only with numerical simulations (see Section 3), but incorporating the cooling timescale into the analytical model should be possible. We also assume that the cavity is only powered by stellar photoionization, since otherwise the cavity is likely to develop a gradient in its density profile or other shocked structures due to the presence of radiation pressure and stellar winds (e.g. Draine 2011).

The density and radius of the molecular cloud are denoted by ρ_{cloud} and r_{cloud} respectively. Cold molecular gas is at around 10 K, and its pressure p_{cloud} is obtained with equation 2. The warm envelope has density ρ_{env} and we assume its temperature to be 10^3 K (cf. Lucas et al. 2017), giving its pressure p_{env} . The shell of swept-up ISM gas surrounding the HII region has thickness δr_{shell} and density ρ_{shell} , hence an initial mass of $M_{\text{shell},0} = \rho_{\text{shell}} 4\pi \delta r_{\text{shell}}^2$. Since the shell expansion has stalled at this point, p_{cloud} and p_{HII} should be approximately equal, though this is not a necessary requirement for our calculations.

Similar to Geen & de Koter (2022), we consider the outflow to occur only from a small solid angle from the progenitor. We model the feedback-carved channel as an opening angle from the HII region. The area of the hole on the shell is hence $s_{\text{out}} = \Omega r_{\text{HII}}^2$, where Ω is the solid angle. However, in this analytical model, s_{out} only controls the total outflow rate from the cavity, and therefore does not distinguish between a wider solid angle and more holes on the shell. This variable is analogous to the shell cover fraction C_f introduced by Harper-Clark & Murray (2009), who incorporated this parameter into the models of wind-blown bubbles (Castor et al. 1975) to account for incomplete confinement. Similarly, Rahner et al. (2017) also modelled the leakages through shells via an escape fraction f_{esc} , though, unlike Fig. 1, they assumed that the leakage does not begin

until the shell reaches the edge of the cloud, or at least a fraction of its total radius if shell fragmentation is taken into account (Rahner et al. 2018).

It is also worth noting that the term s_{out} in our model covers all exposed areas on the shell through which fluid can advect, regardless of its cause. It hence encompasses the existing low-density channels in the cloud and those cleared by pre-SN feedback, as well as the gaps that formed due to gravitational fragmentation (e.g. Whitworth et al. 1994), Rayleigh-Taylor instabilities (e.g. Krumholz et al. 2009; Kumar 2013), or Vishniac instability (e.g. Minière et al. 2018), all of which are highly probable especially during the late evolutionary stages of the bubble. The only requirement is that the area of the vent(s) must be small relative to the cavity volume.

Consider a SN progenitor of total energy $E_{\text{SN}} \sim 10^{51}$ erg contained within an initially small volume V_{SN} , which corresponds to the SN injection radius, located inside the cavity. We can first write down an energy conservation equation,

$$\frac{P_{\text{HII}}}{\rho_{\text{HII}}(\gamma - 1)} \rho_{\text{HII}} (V_{\text{HII}} - V_{\text{SN}}) + E_{\text{SN}} = \frac{P}{\rho(\gamma - 1)} \rho V \quad (3)$$

(cf. Feldgun et al. 2011). The RHS gives the total energy contained within the cavity, whose density, pressure and volume are denoted by ρ , p and V respectively. The initial cavity pressure p can thus be obtained by rearranging equation (3). Its total mass M is given by

$$M = \rho_{\text{HII}} (V - V_{\text{SN}}) + M_{\text{SN}}, \quad (4)$$

where M_{SN} is the total ejecta mass. Combining equation (3) and (4) hence gives an estimate of the energy per unit mass in the cavity, or the SN mass-loading,

$$\epsilon = \frac{1}{M} \frac{P}{\rho(\gamma - 1)} \rho V. \quad (5)$$

This equation assumes that the SN energy is equally distributed amongst the gas within the cavity before the pressure relief phase begins. Following Dwarkadas (2005), we assume that the cavity can be simply regarded as a region of uniform internal energy. This assumption might not hold during initial stages where the shock waves are still oscillating between the shells, but by the end of this brief non-stationary phase, the SN remnant should slowly approach complete thermalization as it collides with the cavity walls (see also Walch & Naab 2015). Thus, as far as pressure relief phase is concerned, the uniform cavity assumption should be appropriate. This is also in line with the ‘spatially lumped gas’ approximation made in Feldgun et al. (2011), that the gas properties *within* the confined volume varies only with time, with no radial or directional dependence.

2.1.2 Shell collision

The first part of our model considers the spherically symmetrical collision between the SN and the circumstellar shell. This problem has been first extensively studied by e.g. Chevalier & Liang (1989); Dwarkadas (2005, 2007), who modelled the dynamics of the shell upon SN impact. Whether or not the evolution of the SN remnant would be significantly affected depends on the mass of the swept-up material relative to the ejecta, which in turn is dependent on the mass loss from the progenitor mainly during its supergiant phase. For simplicity, we adopt the thin-shell approximation, such that $\delta r_{\text{shell}} \ll r_{\text{HII}}$ and the shock front remains attached to the shell’s position. The following calculations are largely based on the work of Dwarkadas (2005, Section 5).

As with many self-similar solutions, the initial velocity of the shell

upon collision with the SN shock can be estimated using dimensional analysis, giving

$$v_{\text{shell},0} = \left(\frac{\beta p}{\rho_{\text{shell}}} \right)^{1/2}, \quad (6)$$

scaled by a constant $\beta \sim 6$ (Chevalier & Liang 1989). The pressure term p in equation (6) originally refers to the post-shock pressure in Chevalier & Liang (1989), but here we will approximate it as the cavity pressure. To understand how the shell would evolve under the pressure imbalance between the bubble and the cloud, we write down an equation of motion,

$$F = M_{\text{shell}}(r) \frac{dv_{\text{shell}}}{dt} = 4\pi r^2 p_{\text{net}}, \quad (7)$$

where p_{net} is the net pressure acting on each side of the shell. The variable r denotes the instantaneous radius of the cavity, and initially, $r = r_{\text{HII}}$. We can rewrite equation (7) as

$$\frac{dv_{\text{shell}}}{dt} = \frac{4\pi r^2}{M_{\text{shell}}(r)} \left(p - \rho_{\text{cloud}} v_{\text{shell}}^2 \right). \quad (8)$$

Note that the mass of the shell in equation (7) and (8) grows as a function of r . This is because as the cavity expands after the collision, the cold gas in the molecular cloud is continuously being swept on to the shell. We model this by, first, considering its mass conservation,

$$\frac{dM_{\text{shell}}}{dt} = 4\pi r^2 \rho_{\text{cloud}} v_{\text{shell}} \quad (9)$$

(cf. Dwarkadas 2005). Integrate by separation of variables gives

$$\int dM_{\text{shell}} = 4\pi \rho_{\text{cloud}} \int r^2 \frac{dr}{dt} dt. \quad (10)$$

With this, the shell mass M_{shell} at current cavity radius r can be expressed in terms of its initial value $M_{\text{shell},0}$,

$$M_{\text{shell}}(r) = M_{\text{shell},0} + 4\pi \rho_{\text{cloud}} \int_{r_{\text{HII}}}^r r'^2 dr' \quad (11)$$

The second term in the above gives the swept-up mass as cavity expands from the initial radius r_{HII} to r . By integrating equation (11), we can arrive at the expression

$$M_{\text{shell}}(r) = M_{\text{shell},0} \left[\frac{M_{\text{rHII}}}{M_{\text{shell},0}} \left(\frac{r^3}{r_{\text{HII}}^3} - 1 \right) + 1 \right], \quad (12)$$

where M_{rHII} denotes the mass of surrounding medium (the molecular cloud) if it had extended from $r = 0$ to $r = r_{\text{HII}}$, given by

$$M_{\text{rHII}} = \frac{4}{3} \pi r_{\text{HII}}^3 \rho_{\text{cloud}}. \quad (13)$$

As long as the cavity is dominated by the pressure from the SN explosion, equation (8) should be sufficient to describe its motion. However, at later times the gravity acting on the shell may be able to exert an inward force and, by the end, drive an implosion that causes the shell materials to once again fill the evacuated cavity (e.g. Romano et al. 2024). Despite the end stages of the SN remnant is beyond the scope of our model, we may roughly account for this by including an extra term to subtract off equation (8),

$$\frac{dv_{\text{shell}}}{dt} = \frac{4}{3} \pi G r \rho, \quad (14)$$

which is the gravitational acceleration towards the centre of the HII region. But note that the simulations presented in this paper do not include self-gravity in order to isolate the effect of SN pressure.

2.1.3 Outflow rate

The second part of the calculations considers the venting of gas from the cavity into the outer envelope. A simple model has been proposed by Feldgun et al. (2011) for modelling interior explosions within containers that has a flexible cover – we apply their approach to tackle our problem. We assume that the SN energy is only permitted to leave through a channel, and there is no energy loss via thermal conduction from the cold shell (e.g. Keller et al. 2014) or turbulent mixing at the bubble-ISM interface (e.g. Geen et al. 2023). The only goal is to gauge the effects of limiting SN outflows to certain particular direction(s).

Consider a streamline that leads from the inside of the cavity, just beneath the cloud’s radius as marked by the red cross in Fig. 1, to an arbitrary point in the outer warm envelope. All outflows from the cavity follow this streamline, and we make the crude approximation that there is no energy loss and no development of Kelvin–Helmholtz instability along the flow. We also assume that the gas behaves adiabatically, and thus obeys Poisson’s adiabatic equation, $pV^\gamma = \text{Const.}$, which implies that the relation

$$p \propto V^{-\gamma} \propto \rho^\gamma \quad (15)$$

would hold at any arbitrary point along the stream. The streamline flow is also governed by the Bernoulli equation,

$$\frac{v'^2}{2} + \Pi(p') = \text{Const.}, \quad (16)$$

where v' is the velocity of the flow at an arbitrary point along the stream, p' is its pressure, and $\Pi(p')$ is the potential energy per unit mass at this point. The starting point of the stream located just inside the cavity therefore has pressure p , density ρ , and velocity v_{out} – these are the properties at the detector that we aim to calculate. The end point of the stream in the envelope has pressure p_{env} , density ρ_{env} , and velocity v_{env} . Following Feldgun et al. (2011), we consider the end point to be the ‘reference point’ in the flow, and evaluate the potential energy term Π in equation (16) as the *pressure energy* per unit mass. The potential energy at a certain point along the stream (denoted by the subscript c) is hence given by

$$\Pi(p_c) = \int_{p_c}^{p_{\text{env}}} \frac{1}{\rho(p')} dp', \quad (17)$$

where the lower limit in the integral is the pressure at this particular point, p_c , and the upper limit is the pressure at the reference point that was defined to be p_{env} . Combining equation (16) and (17), we can now write down an equation that relates the gas properties at the two ends of the stream,

$$\frac{v_{\text{out}}^2}{2} + \int_p^{p_{\text{env}}} \frac{1}{\rho(p')} dp' = \frac{v_{\text{env}}^2}{2} + \int_{p_{\text{env}}}^{p_{\text{env}}} \frac{1}{\rho(p')} dp', \quad (18)$$

since $p_c = p$ at the starting point and $p_c = p_{\text{env}}$ at the end point. The integral term in the RHS can then be eliminated.

The trick to solve equation (18) is to define the end point of the streamline to where the velocity of the flow drops to zero, i.e. $v_{\text{env}} = 0$. This further simplifies the equation to

$$\frac{v_{\text{out}}^2}{2} + \int_p^{p_{\text{env}}} \frac{1}{\rho(p')} dp' = 0. \quad (19)$$

We may now also use Poisson’s adiabatic relations (equation 15) to relate the density and the pressure of the cavity, which is the stream starting point, to that of the envelope,

$$p = p_{\text{env}} \left(\frac{\rho}{\rho_{\text{env}}} \right)^\gamma. \quad (20)$$

This equation can then be rearranged to give an expression for $\rho(p)$. Substituting it into equation (19) and integrate by change of variables, we can arrive at the equation,

$$\frac{v_{\text{out}}^2}{2} + \frac{\gamma}{\gamma - 1} \frac{p_{\text{env}}}{\rho_{\text{env}}} \left[1 - \left(\frac{p}{p_{\text{env}}} \right)^{\frac{\gamma-1}{\gamma}} \right] = 0 \quad (21)$$

(cf. Feldgun et al. 2011). Finally, rearranging equation (21) gives the velocity at the starting point of the stream, i.e. the outflow velocity from the channel,

$$v_{\text{out}} = \sqrt{2 \frac{\gamma}{\gamma - 1} \frac{p_{\text{env}}}{\rho_{\text{env}}} \left[\left(\frac{p}{p_{\text{env}}} \right)^{\frac{\gamma-1}{\gamma}} - 1 \right]}. \quad (22)$$

As the gas leaks through the channel, the mass loss rate from the bubble may be estimated as

$$\frac{dM}{dt} = \rho_{\text{env}} v_{\text{out}} s_{\text{out}} \quad (23)$$

where s_{out} is the total area of the hole(s) on the shell.

Note that because the expression of v_{out} (equation 22) varies only with the instantaneous cavity pressure p (assuming that envelope properties remain constant), it does not require whether s_{out} is formed of a single hole or multiple smaller holes. For the latter case, this model predicts the same v_{out} in outflows from all vents, though, of course, the mass loss rate (equation 23) would be higher. However, these vents must be sufficiently small for the outflows to be considered as a single streamline, which otherwise the use of Bernoulli equation would be invalid. As such, our model cannot account for massive bulk outflows in the case of very large openings. Furthermore, there may be non-linear effects when outflows through different channels interact with each other. Since the above calculations are independent of the orientation of the vents, this scenario may only be tested using 3-D numerical simulations.

2.1.4 Adiabatic pressure relief

The third part considers the rate of pressure decay in the cavity as the SN energy leaves. We make a crude assumption that the energy per unit mass within the cavity, as initially deposited from the SN, remains the same throughout the evolution. We also assume that the Poisson’s adiabatic relation (equation 20) governing the streamline continues to hold during this pressure relief phase. As the cavity radius increases (equation 8) and the mass drops (equation 23), we update the cavity pressure using its current mass M and radius r ,

$$p = \epsilon (\gamma - 1) \frac{M}{V} \quad (24)$$

where $V = 4/3\pi r^3$ and ϵ is from equation (5). Substituting this into the Poisson’s adiabatic relation gives the new cavity density,

$$\rho = \rho_{\text{env}} \left(\frac{p}{p_{\text{env}}} \right)^{1/\gamma}. \quad (25)$$

Finally, we put all equations described in Section 2.1.1, 2.1.2, 2.1.3 and 2.1.4 together and evolve this system of equations numerically to give the time-evolution of gas properties at the detector. The steps to initialize the parameters and the way to update them in each time-step are summarized in table 1 and 2. Here, we adopt a simple Eulerian integrator to evolve the parameters. Using velocity Verlet or Runge-Kutta integrators would be more ideal, but no numerical stability issues have been encountered so far. The calculation outputs are presented in Section 4.3 to compare against the results from 3-D

Table 1. Algorithm to initialize the analytical model of a semi-confined SN

Procedure	Equation
Calculate initial pressure p	3
Calculate initial mass within cavity M	4
Calculate mass loading ϵ	5
Initiate r by setting it to r_{HII}	
Calculate initial shell velocity v_{shell}	6

Table 2. Algorithm to evolve the analytical model of a semi-confined SN

Procedure in each time-step dt	Equation
Calculate $v_{\text{out}}(p)$	22
Calculate dM/dt	23
Update $M = M - \frac{dM}{dt} dt$	
Calculate mass of shell + mass swept M_{shell}	12
Calculate acceleration of shell dv_{shell}/dt	8
Update velocity $v_{\text{shell}} = v_{\text{shell}} + (dv_{\text{shell}}/dt) dt$	
Update cavity radius $r = r + v_{\text{shell}} dt$	
Calculate cavity pressure p	24
Calculate cavity density ρ	25

hydro simulations. We will show that this analytical model is capable of predicting the outflow properties in spite of the approximations and simplifications made in the calculations.

2.2 Free-field supernova

We now turn to model the outflows from a free-field SN, where there is no preferential energy escape route. The explosion occurs within a uniform ambient medium of density ρ_{amb} . To allow for comparisons with the semi-confined model, we consider a detector that is placed at the same distance away from the progenitor, as indicated in Fig. 1. We model the evolution of gas properties at the detector after the SN shock front has passed through it, meaning the detector is located in the post-shock region. Since the blast is now spherically symmetrical, the well-established self-similar shock wave equations apply. The Sedov-Taylor solution (Sedov 1946; Taylor 1950) gives the velocity of the shock front v_{shock} as a function of its radius r_{shock} ,

$$v_{\text{shock}} = \frac{2}{5} \xi_0^{5/2} \left(\frac{E_{\text{SN}}}{\rho_{\text{amb}}} \right)^{1/2} r_{\text{shock}}^{-3/2} \quad (26)$$

where ξ_0 is a dimensionless variable. For $\gamma = 5/3$, we can assume $\xi_0 \sim 1.15$ Ostriker & McKee (1988).

To determine the properties behind this shock front, we first define a scale-free radius η ,

$$\eta = \frac{r_0}{r_{\text{shock}}} \quad (27)$$

(cf. Díaz & Rigby 2022), where r_0 denotes the position of the detector ($r_0 < r_{\text{shock}}$). The gas velocity, density and pressure at the detector are denoted by v_0 , ρ_0 and p_0 respectively. These properties can be calculated by applying the Rankine-Hugoniot relations (Rankine 1870; Hugoniot 1887). These relations are formed based on boundary conditions on the hydro equations at the shock front discontinuity, derived from the conservation of mass, energy and momentum. In terms of variables considered in our model, the solutions read:

$$\frac{v_0}{v_{\text{shock}}} = \frac{\eta}{\gamma} + \left(\frac{\gamma - 1}{\gamma^2 + \gamma} \right) \eta^\alpha, \quad (28)$$

Table 3. Algorithm to evolve the analytical model of a free-field SN

Procedure in each time-step dt	Equation
Calculate v_{shock}	26
Update $r_{\text{shock}} = r_{\text{shock}} + v_{\text{shock}} dt$	
Calculate η	27
Calculate M_s	32
Calculate v_0 , ρ_0 and p_0	28,29,30

$$\frac{\rho_0}{\rho_{\text{amb}}} = \left(\frac{\gamma + 1}{\gamma - 1} \right) \frac{\eta^b}{\gamma^c} \left(\gamma + 1 - \eta^{a-1} \right)^c, \quad (29)$$

$$\frac{p_0}{p_{\text{amb}}} = M_s^2 \left(\frac{2\gamma^{1-d}}{\gamma + 1} \right) \left(\gamma + 1 - \eta^{a-1} \right)^d, \quad (30)$$

with the exponents given by

$$a = \frac{7\gamma - 1}{\gamma^2 - 1}, \quad b = \frac{3}{\gamma - 1}, \quad c = \frac{2\gamma + 10}{\gamma - 7}, \quad d = \frac{2\gamma^2 + 7\gamma - 3}{\gamma - 7} \quad (31)$$

(cf. Díaz & Rigby 2022, equation 16-19). The Mach number M_s in equation (30) is given by the ratio of shock velocity to the sound speed,

$$M_s = \frac{v_{\text{shock}}}{c_s}, \quad (32)$$

where $c_s = \sqrt{\gamma p_{\text{amb}} / \rho_{\text{amb}}}$. We assume that the above relations hold throughout the Sedov phase, and we do not consider its transition to the snowplough phases to be consistent with the adiabatic assumptions used in our semi-confined model.

Similar to before, we evolve the equations numerically to solve for the time-evolution of the gas properties. The shock radius r_{shock} begins at the position of the detector r_0 . The subsequent steps to evolve the system are summarized in table 3. The calculation results are presented in Section 4.3 to compare against the semi-confined model and the results from 3-D numerical simulations.

3 NUMERICAL METHODS

We perform 3-D Smoothed Particle Hydrodynamics (SPH) simulations (Gingold & Monaghan 1977; Lucy 1977) to test our analytical models as well as to further examine the differences between free-field SN and semi-confined SN. SPH is a Lagrangian particle-based method that solves the equations of hydrodynamics by discretizing the fluid into individual particles, each serving as an interpolation (sampling) point of the underlying fluid properties. The simulations are carried out with the SPH code PHANTOM, developed by Price et al. (2018), which adopts a variable smoothing length formalism with equal mass particles. Shock discontinuities are treated with artificial viscosity and artificial thermal conductivity (Chow & Monaghan 1997; Price 2008). Here, we neglect the self-gravity of the particles.

3.1 Supernova model

Supernova is injected by adding extra particles whose total mass corresponds to the ejecta mass, which we roughly assume to be a quarter of that of the progenitor. The extra particles carry a total energy of approximately 10^{51} erg, and are randomly (but symmetrically across

the Cartesian axes) positioned within a sphere of r_{SN} , which we define to be 0.1 pc. The split of thermal to kinetic energy may vary in each run. For kinetic energy injections, the ejecta particles' radial velocities are set in the form of a skewed Gaussian function². The purpose is to allow the particles closer to the centre to catch up with those further away and thus forming a shell, while also leaving some particles behind to avoid completely evacuating the centre, which can lead to poor resolution in SPH.

Radiative cooling is incorporated using the cooling curve of [Joung & Mac Low \(2006, Fig. 1\)](#). Cooling curves are pre-computed cooling rates Λ as a function of gas temperature T that replace on-the-fly chemistry calculations. This method is largely appropriate as far as gas dynamics is concerned. Here, the [Joung & Mac Low \(2006\)](#) curve assumes ionization equilibrium and is applicable to optically thin plasmas with solar metallicities. The high temperature regime of the curve ($T \geq 2 \times 10^4$ K) is from [Sutherland & Dopita \(1993\)](#) and the low temperature regime ($T < 2 \times 10^4$ K) is from [Dalgarno & McCray \(1972\)](#) for an ionization fraction of 10^{-2} .

Following [Koyama & Inutsuka \(2002\)](#), we also apply a small constant heating term, $\Gamma = 2 \times 10^{-26}$ erg s⁻¹, which covers the heating from external cosmic rays and FUV fields ([Wolfire et al. 1995](#)). The internal energy u of each particle is subsequently updated using an implicit method introduced by [Vazquez-Semadeni et al. \(2007\)](#),

$$u_{i+1} = u_{\text{eq}} + (u_i - u_{\text{eq}}) \exp\left(-\frac{dt}{\tau}\right), \quad (33)$$

where i denotes an arbitrary hydro step and dt is the time-step. u_{eq} is the internal energy that corresponds to the particle's equilibrium temperature. The u_{eq} values are pre-computed by solving the thermal equilibrium, $n_H \Gamma - n_H^2 \Lambda(T) = 0$, where n_H is the hydrogen number density³. The equilibrium temperatures as a function of density ρ are plotted in Appendix A. τ is the timescale over which the gas particle radiates its thermal excess, given by

$$\tau = \left| \frac{u - u_{\text{eq}}}{n_H \Gamma - n_H^2 \Lambda} \right| \quad (34)$$

(cf. [Vazquez-Semadeni et al. 2007](#)). The use of implicit methods directly corrects the particle internal energy by the end of each hydro step and prevents the time-step from being overly constrained as the SN shock cools. This cooling method has also been used in [Bonnell et al. \(2013\)](#) to account for the bi-stable nature of ISM temperatures.

3.2 Photoionization

We incorporate stellar photoionization by employing the hybrid tree-based radiation hydrodynamics (RHD) scheme described in [Petkova et al. \(2021\)](#); [Lau et al. \(2024\)](#). This RHD scheme couples the SPH code PHANTOM to a grid-based Monte Carlo Radiative Transport (MCRT) code CMACIONIZE ([Vandenbroucke & Wood 2018](#); [Vandenbroucke & Camps 2020](#)) to model the thermodynamical impact of ionizing radiation in SPH. It works by transferring the particle-interpolated densities on to a Voronoi grid ([Voronoi 1908](#)) at each hydro step with the Exact density mapping method ([Petkova et al. 2018](#)), and executing the MCRT simulation on this Voronoi density

² We borrow the functional form of the 1st derivative of the SPH cubic B-spline kernel ([Schoenberg 1946](#)) to set the radial velocity profile. The code scales the amplitude during runtime such that the total kinetic energy carried by the SN ejecta particles matches the required value.

³ This property relates to the particle density ρ by $n_H = \rho/m_H$, where m_H is the hydrogen mass.

field to compute the ionic fraction of each cell. The results are subsequently returned to PHANTOM for computing the photoionization heating and cooling rates for each particle. This scheme also employs a tree-based optimization algorithm that adaptively converts gravity tree nodes into pseudo-SPH particles, with which we carry out the mapping, allowing resolutions to be lowered in the neutral regions. We use this method to self-consistently generate expanding HII regions in our simulated molecular clouds that sweep its surrounding gas into thin but dense shells, replicating the scenario shown in Fig. 1.

4 RESULTS

Two sets of simulations are presented – one as an adiabatic test, and one with radiative cooling incorporated. The early stages of SN evolution may be approximated as an adiabatic process, but radiative cooling soon begins to dominate after the remnant reaches its snowplough phases. We anticipate the adiabatic results to match the predictions derived from the analytical models, whereas the results from the cooling runs would provide useful information on their realistic impact. Parsec-scale simulations usually do not suffer from numerical overcooling, nevertheless it may be assumed that the ‘true’ effect would lie somewhere in between the two test cases. Fig. 2 illustrates the evolution of a semi-confined SN in the adiabatic run and in the cooling run. The particle density-weighted column internal energies are plotted, and the geometrical features seen in the images correspond to the depiction in Fig. 1. It is apparent that the Mach number of the outflow is significantly higher in the adiabatic test which leads to the formation of bow shocks. We describe below the details on the simulation setup and starting conditions.

4.1 Simulation initial conditions

4.1.1 Adiabatic

The semi-confined SN setup in the adiabatic runs consist of a spherical molecular cloud of radius $r_{\text{cloud}} = 25$ pc and density $\rho_{\text{cloud}} = 10^{-21}$ g cm⁻³ with temperature $T_{\text{cloud}} = 10$ K. Its mass is hence approximately $10^6 M_{\odot}$. No turbulence is added to the molecular cloud, consistent with the analytical model. The mass resolution is $10^{-1} M_{\odot}$.

The HII region is evolved until the ionization front reaches approximately $r_{\text{HII}} = 10$ pc, a typical (minimum) radius of a feedback-driven cavity found in studies by e.g. [Dale et al. \(2014\)](#); [Fichtner et al. \(2024\)](#). The ionized gas temperature is at around 10^4 K once in thermal equilibrium, and has density $\rho = 10^{-22}$ g cm⁻³, slightly lower than that of the cloud ISM due to the thermal pressure. According to the simulation results, the swept-up shell reaches a density of around $\rho_{\text{shell}} = 10^{-19}$ g cm⁻³, with thickness $\delta r_{\text{shell}} = 0.5$ pc. The outer envelope has density $\rho_{\text{env}} = 4 \times 10^{-25}$ g cm⁻³ and a temperature of 10^3 K.

A channel is manually carved by randomly deleting 90% of the particles that lies within the cone drawn by a small solid angle, $\Omega = 0.1 \times 4\pi$, from the location of the progenitor up to the radius of the cloud. A caveat to note is that doing this effectively reduces the fluid resolution along the channel(s), which might lead to ambiguous results regarding the gas flows around these holes. This issue has also been noted in [Dale & Bonnell \(2008\)](#) and is likely a common issue with modelling voided regions in SPH. The detector, as illustrated in Fig. 1, is placed at 25 pc from the progenitor at the opening of this channel.

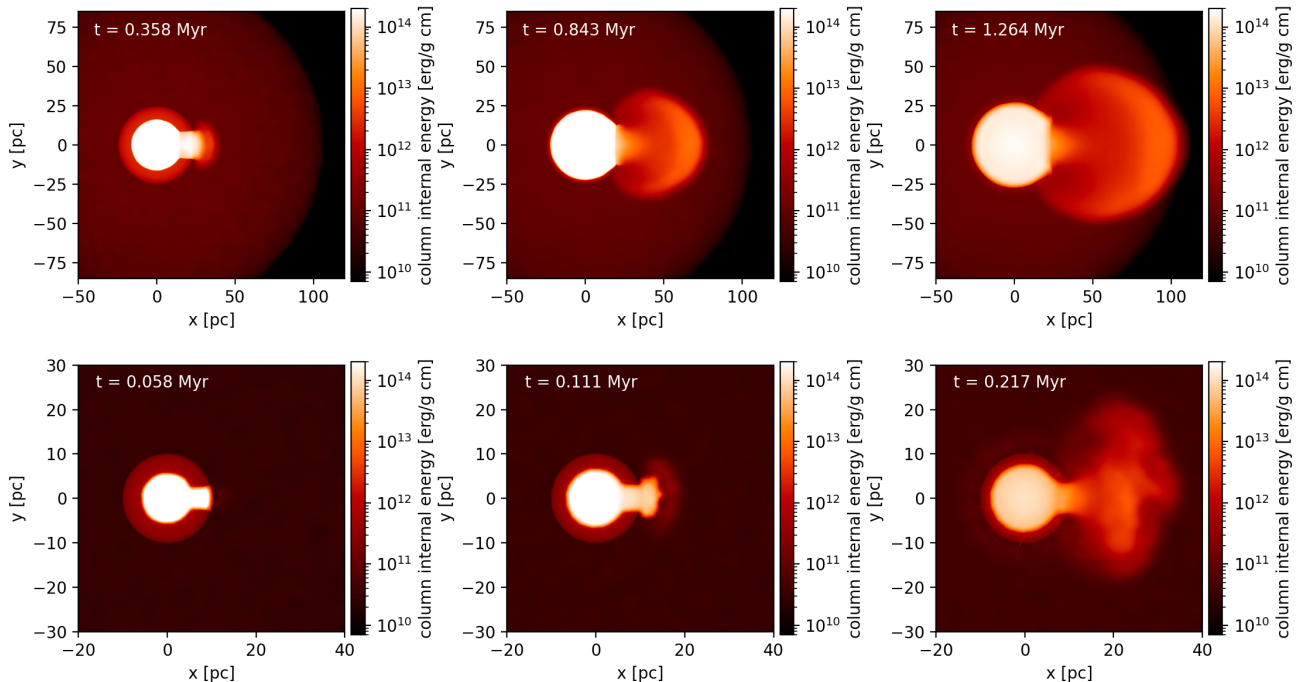


Figure 2. *Left to right:* Evolution of the semi-confined SN from 3-D hydrodynamical simulations in the adiabatic run (*top*) and in the cooling run (*bottom*). The render shows the density-weighted column internal energy interpolated from the SPH particles. The high-energy SN remnant within the cavity is mostly in white, surrounded by a spherical molecular cloud that is seen as a ring. The warm envelope is seen as the faint background with circular boundaries.

For the free-field case, the density of the ambient medium here is set to be the same as that of the warm envelope in the semi-confined case, so $\rho_{\text{amb}} = 4 \times 10^{-25} \text{ g cm}^{-3}$. A higher density could have been used if the medium represents a smeared molecular cloud, however, we conjecture that a denser medium would only further restrict the propagation of the shock which results in weaker outflows. Hence, testing a free-field SN in a low-density medium provides the upper limit in the strength of its outflows in a particular direction.

In both runs, the SN is injected as pure thermal energy. This was done to comply with the assumption made in our analytical model that the SN energy has completely thermalized after the remnant collides with the walls of the cavity. Since the simulation is adiabatic, this energy is not lost and will only be converted into kinetic energy as it drives the shock. The SN energy is distributed to 700 ejecta particles injected into the simulation, each carrying the same mass as the gas particles. We evolve the simulation for approximately 3 Myr after the SN detonation; beyond this point the cloud itself becomes largely destroyed by the hot remnant.

4.1.2 With-cooling

To avoid the SN energy from being completely dissipated before an outflow is driven out of the cavity, we use a smaller cloud, which reduces the length-scales and the timescales compared to the adiabatic runs. The molecular cloud has radius $r_{\text{cloud}} = 10 \text{ pc}$ and density $\rho_{\text{cloud}} = 10^{-21} \text{ g cm}^{-3}$. This gives a total mass of around $6 \times 10^4 M_{\odot}$. The mass resolution is increased to $10^{-2} M_{\odot}$ to further suppress the spurious cooling from under-resolved high densities. The HII region is evolved to radius $r_{\text{HII}} = 4 \text{ pc}$. This radius is much smaller than the typical cavity size but could represent that of an earlier epoch, say around 6 Myr from the onset of feedback (cf. Dale et al. 2014, Figure

1), which is well sufficient for the most massive stars to explode as SN.

The thickness of the shell was found to be around $\delta r_{\text{shell}} = 0.2 \text{ pc}$ with density $\rho_{\text{shell}} = 10^{-19} \text{ g cm}^{-3}$. We further manually reduce the density of the evolved HII region in order to moderately suppress the amount of cooling within the cavity. This is done by replacing the particles within the shell’s inner boundaries with a new set of uniformly-distributed particles at temperature 10^4 K and density $\rho = 10^{-23} \text{ g cm}^{-3}$. Applying this procedure may lead to some inconsistencies in the gas evolution, but we argue that a lower density cavity is justified since, in reality, the bubbles are also subjected to stellar winds that drive materials out of the cavity. It does not affect the credibility of this simulation for testing our analytical models, given that the pressure difference between the cavity and the envelope is the only determining factor.

The density of the warm envelope is $\rho_{\text{env}} = 4 \times 10^{-25} \text{ g cm}^{-3}$. With radiative cooling applied, the particle’s equilibrium temperatures are governed by its density. However, they should remain similar to those in the adiabatic runs since the cloud and envelope densities were chosen to match our desired temperatures (see the equilibrium temperature plot Fig. A1 in Appendix A). A channel is emptied with a similar method described in Section 4.1.1, and the detector placed at 8 pc from the progenitor.

The SN is injected as pure kinetic energy. This is because (a) otherwise cooling would artificially dissipate a significant portion of the injected energy before the particles relax, and (b) it has been revealed that, within 5 pc, the majority of the SN energy should be still in kinetic form (Fichtner et al. 2024). It is only beyond this radius that the energy is starting to be converted into thermal energy via shock heating. We evolve the simulation only up to around 0.3 – 0.4 Myr after the SN detonation, since after that the remnant cools and is no longer driving shocks in its outflows.

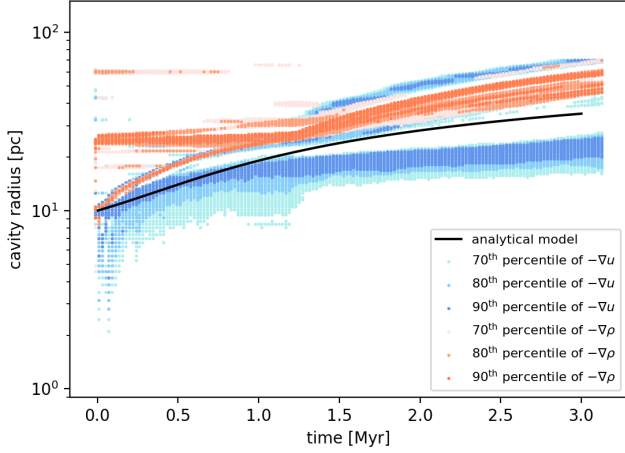


Figure 3. Expansion of cavity shell radius upon collision with the SN shock in the adiabatic test. Prediction from the analytical model is plotted in black. The shell location in the simulation is traced by large negative gradients in density (red) or in internal energy (blue) along a 1-D line from the progenitor. Colours indicate the percentile of the gradient, with darker colours indicate steeper falls. The cloud has radius 25 pc, and its boundary is seen as the horizontal features in the density gradients. The simulation terminates at around 3 Myr.

4.2 Shell expansion

We first examine whether or not the predicted evolution of cavity radius r in our semi-confined model (Section 2.1.2) matches that from the simulations. An issue is that the boundaries of the shell or shock front in the simulation may become ambiguous due to the multiple shock waves produced from collisions between the SN and the cold molecular cloud gas. This is particularly severe in the adiabatic runs, in which the shock front extends significantly beyond the initial boundaries of the cloud itself. Furthermore, their outflows from the channel were seen to induce reverse shocks that wrapped around the other regions of the cloud and interfered with the expanding cavity. All of these factors complicate the geometry of the shell in our simulations.

As such, we resolve to estimate the location of the shock front(s) by locating regions where large gradients in density and/or internal energy are present. We do so by, first, defining a straight line along the negative x -axis, radially away from the progenitor and opposite to the channel. Equally-spaced interpolation points are set along the line, and we measure the density and internal energy of the fluid via interpolation from neighbouring particles. From this, we obtain the density and internal energy gradients along the line, and extract the radii with the steepest gradients. The results are shown Fig. 3 and 4.

Fig. 3 plots the radii in the adiabatic run whose negative gradients in density and internal energy lie in their 70th-, 80th- and 90th-percentile, giving a 1-D contour map of the shock at each time-step. It highlights one side of the compressed wave. We choose to display the negative gradients rather than the positive since the negative component appears to be a better tracer of the shell boundary, whereas the positives are heavily contaminated by the energy distribution of the SN remnant itself. Note that the horizontal features seen at the early times in density gradients are the transition regions from the cloud to the envelope.

We plot on top of this contour the results computed with our analytical model. The overall shape of the curve agrees well with the shell domain traced by the density gradients. The large gap seen in the internal energy negative gradients indicates that internal energy tends to rise sharply and builds up at the inner cavity walls. The fact

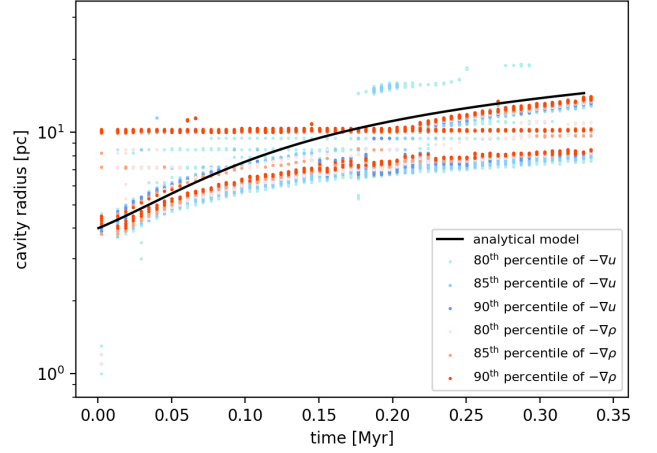


Figure 4. Same as Fig. 3 but for the run with radiative cooling included in the simulation. The cloud has radius 10 pc, and is responsible for the horizontal features seen at 10 pc. The simulation terminates at around 0.3 Myr, much shorter than that in Fig. 3 due to the reduced size-scales in the setup. The analytical model (black) is computed using parameters described in Section 4.1.2 but does not account for cooling effects.

that the curve lies mostly along this gap arguably serves as an extra proof of our analytical model.

We repeat the same procedures for the with-cooling run, as shown in Fig. 4. We plot the radii whose negative gradients in density and internal energy lie in their 80th-, 85th- and 90th-percentile. Note the difference in time-scales. In this plot, the curve appears to be over-predicting the radius of the shell, assuming that it is predominantly traced by negative density gradients. This result is not surprising, since radiative losses could significantly weaken the strength of the shocks and thus reduce its ability to push against the cavity walls. The gap in internal energy is also much less prominent compared to the adiabatic run, which likely indicates that the SN energy becomes more uniformly distributed within the cavity when the shocks are allowed to cool.

One aspect to note from both Fig. 3 and 4 is that, immediately after the SN explosion, the cavity radius undergoes a rapid expansion followed by a sudden deceleration before transitioning into a steady rise. Despite our model successfully predicts the overall trend, this behaviour was not being reproduced. The reason likely lies in our assumption that the SN energy has already reached a quasi-steady state by the time the gas venting begins, and the direct pressure exerted by the SN was not being taken into account.

4.3 Outflows

We turn to look at the evolution of gas properties at the detector in the outflow, as illustrated in Fig. 1. It provides information on the *local* perturbation after the shock front passes through the area. If one thinks of a sub-grid model as a black box which encapsulates the volume within the cloud's boundaries, then these results would indicate the disturbance in the gas within the box after the energy has escaped to the outer ISM. They also show the strength of the outflow at the box boundary.

Here, we compare three different physical properties: the velocity v (equation 22 from semi-confined model and 28 from free-field model), the thermal pressure p defined by equation (2) (equation 24 from semi-confined model and 30 from free-field model), and ram pressure $p_{\text{ram}} \approx \rho v^2$. These properties are obtained via an interpola-

tion from neighbouring particles around the detector. Note also that, in our analytical model, the ‘spatially lumped’ assumption asserts that the cavity pressure p remains the same throughout the channel – from the cavity interior to where it interfaces the warm envelope. As such, the detector placed in the simulation can be located anywhere along the channel. In our tests, we set it to halfway along the tube. The detector location does not move to follow the expansion of the cavity, but remains within the spatial domains of the channel.

Fig. 5 plots the evolution for the adiabatic runs, synchronized at the time when the shock front arrives at the detector. For each property, we also show the results from the analytical model, computed by substituting the parameter values stated in Section 4.1.1 into the procedures from tables 1, 2 and 3. We see from Fig. 5 first panel that the gas velocities measured at the detector agree well with their predicted values for the semi-confined case. This result validates our analytical model, and demonstrates that outflows from an opening on the bubble can indeed be treated as a single streamline. The gas velocities are initially slightly higher than predicted due to the direct impact from the SN shock, which was not being considered in our calculations. The decay rate is slightly higher than our analytical model, and we attribute this to the expansion of the channel’s cross-sectional area as the energy leaves the cavity. Formulating a method to describe its evolution as a function of v_{out} would be ideal.

As for the free-field, strong agreement has been achieved with the blast wave solutions, as seen in the first panel of Fig. 5. The oscillations likely originate from collisions with the sparsely distributed SPH particles in the ambient medium. More importantly, their velocities at the detector are significantly lower than the semi-confined case. Keeping in mind that the velocities here are that of the post-shock region, a lower velocity does not necessarily imply a slower shock front or a weaker outflow. However, it *does* imply that the local ISM is being relatively less perturbed after the shock front has swept through the area. From this panel, we see that the outflows from the semi-confined case deposits a larger fraction of the injected momentum at smaller length-scales (here ~ 25 pc, the detector distance) compared to the free-field. Their slower rate of decay also imply a more extended momentum deposition timescale.

The second panel in Fig. 5 models the pressure relief from the confined cavity. Similar to before, we find good agreement between the simulated results and the analytical model. It also means that the thermal pressure retained at regions near the progenitor is much higher than if the remnant is freely expanding, limiting the spatial extent of the SN impact. Harper-Clark & Murray (2009) and Lopez et al. (2011) proposed that physical leakages are the primary cause of the X-ray gas pressure loss in the feedback-driven bubbles. Indeed, this is likely the case compared to a fully confined bubble. However, our results here suggest that as long as the bubble is predominantly confined, the rate of pressure loss is not significant. Likewise, ram pressure is also being sustained at a high level, as shown in the third panel. The systematic offset between the measured and the predicted curve is likely only due to the channel density being overestimated. Overall, these results indicate that 1-D models which do not account for partial confinement effects could underestimate the local momentum deposition at small radii from the SN.

The plots for the runs with radiative cooling are shown in Fig. 6. It is apparent that, here, the free-field curves deviate significantly from their predictions obtained from the 1-D blast solutions. This is an inevitable consequence of the cooling, since it removes a significant portion of the energy from the SN after the shock thermalizes and subsequently terminates its Sedov phase. As seen from the second panel, the free-field thermal pressure begins to fall at around 0.15 Myr when radiative cooling starts to dominate. However, this

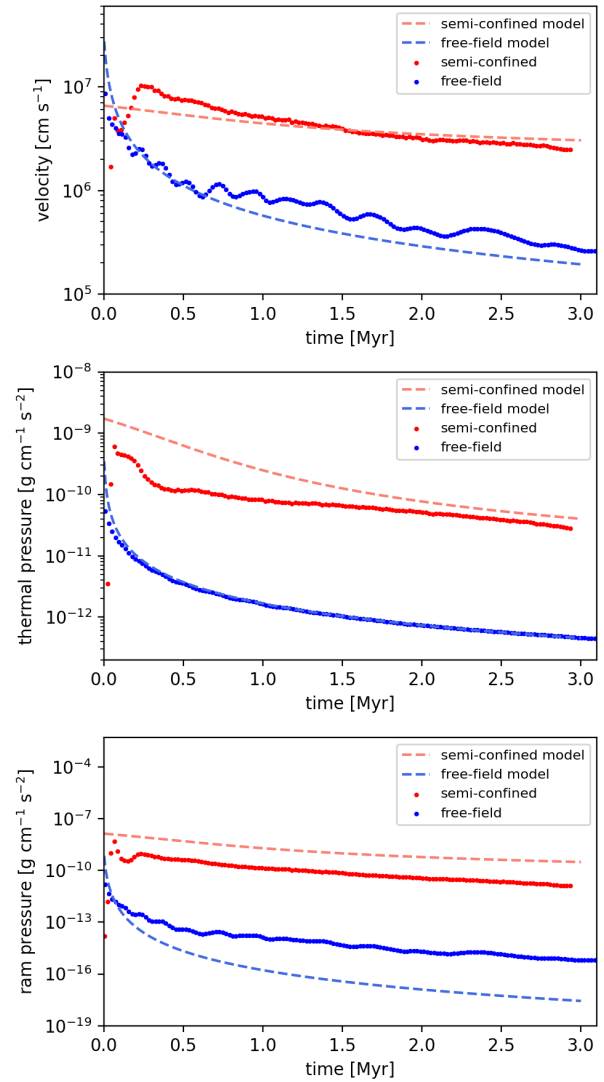


Figure 5. Gas velocity, thermal pressure and ram pressure measured at the detector location from the adiabatic simulation, plotted for the semi-confined case (red) and the free-field case (blue). The curves are synchronized at the time when the shock front arrives at the detector. The results from the analytical models are shown in dotted lines for comparison. The simulation terminates at around 3 Myr.

still does not explain why the gas velocities level out (see first panel) instead of decaying like Fig. 5 after the shock front leaves. We suggest two other factors that are at play: the velocity profile of the ejecta particles that results in a more extended shock, and the gas equilibrium temperatures from our heating and cooling implementations. A detailed explanation is provided in Appendix B.

To the contrary, the gas velocities in the semi-confined case agree very well with the analytical model. Setting aside the systematic offsets caused by overestimated densities, the thermal and ram pressures also show good agreement with their predicted evolutions. This implies that adiabatic assumptions may be applicable for modelling flows through low-density channels where cooling is inefficient. More importantly, our results show that semi-confined SNe can induce stronger and more sustained perturbations to its local environment even when the gas is subjected to radiative cooling.

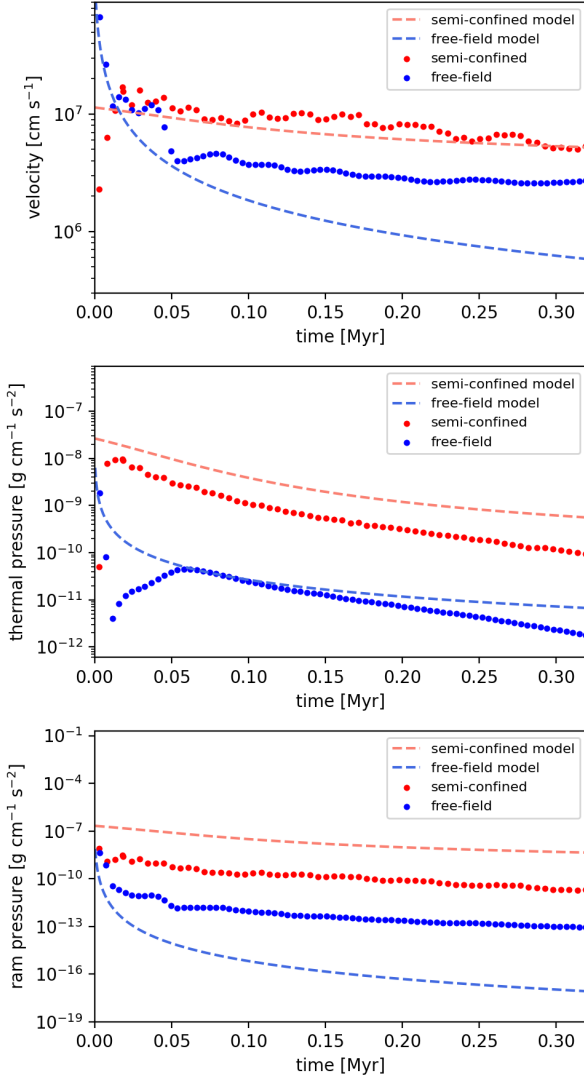


Figure 6. Same as Fig. 5 but for the simulation with radiative cooling. The simulation terminates at around 0.3 Myr.

4.3.1 Multiple channels

It is also possible to assess the effect of increasing the number of channels. In Fig. 7 and 8 we plot the evolution of gas velocities at the detector in four sets of simulations, in which the molecular clouds have one to four identical channels respectively, adiabatic and with cooling. Each channel is carved with the same method described earlier, along four different Cartesian axes relative to the progenitor. The detector is placed in front of one of the channels. Because the setup is geometrically symmetric, the same results would be obtained independent of which channel the detector is placed.

We also plot the predictions calculated with the analytical models. Their results suggest that a small increase in size of the vent imposes negligible effect on the pressure relief. This prediction seems counter-intuitive, that the energy and pressure reduction within the cavity is independent of the number of channel(s) present around the bubble. Indeed, there is a possibility that this is merely a consequence of our small-vent assumption used in the derivations. However, the results obtained from simulations appear to suggest that the model predictions are in fact correct, despite that the channel sizes are

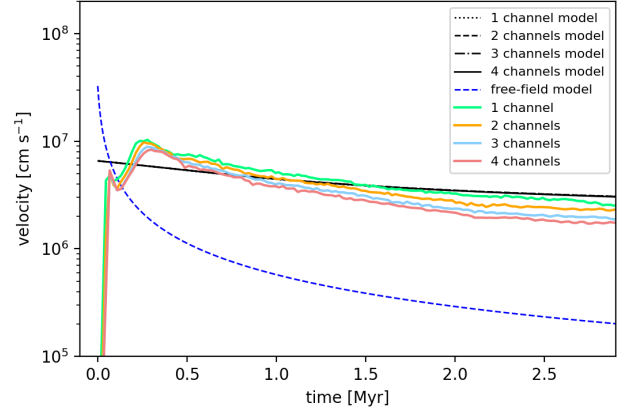


Figure 7. Velocity of outflow gas measured at the detector location from the adiabatic runs, with one to four channels carved around the progenitor, each with solid angle $\Omega = 0.1 \times 4\pi$. The green curve is identical to the semi-confined velocity curve (red) in Fig. 5. Predictions from the analytical model with the corresponding channel sizes are plotted in black for comparison. The free-field curve is shown for reference.

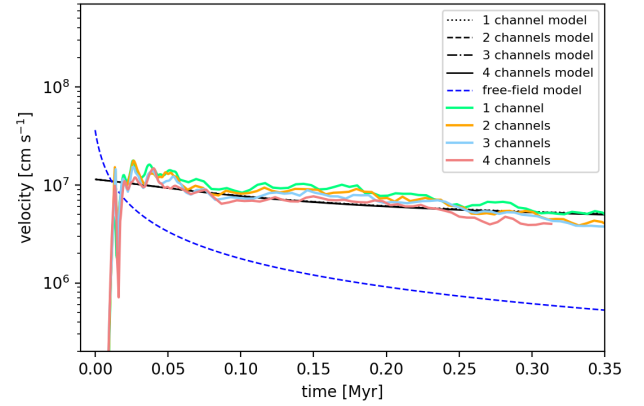


Figure 8. Same as Fig. 7 but for the runs with radiative cooling. The green curve is identical to the semi-confined velocity curve in Fig. 6.

expanding and the outflows are interacting with each other. All curves remain close to the one-channel curve in both the adiabatic and the cooling run; only small differences are seen due to the higher mass loss rate. The results show that our simple analytical model is capable of largely reproducing the behaviour of outflows from bubble leakages.

4.4 Energy deposition

This section examines the coupling efficiency between the energy from semi-confined SNe and their surrounding medium. Fig. 9 plots the kinetic and thermal energy contained within a radius of 20 pc, 50 pc, 80 pc and 100 pc around the progenitor in the adiabatic run. Their total energies are shown in dashed lines. We further include simulations of semi-confined SNe with a larger channel, solid angle $\Omega = 0.3 \times 4\pi$, to examine its effect. We do not experiment with channels any larger than this since, beyond it, the SN outflows no longer exhibit behaviour as vent flows, but rather as a bulk advection. It is apparent from Fig. 9 that the SN energy escapes more quickly in the free-field case than in the semi-confined case across all radii, particularly in its kinetic energy. Semi-confined SN is more capable of retaining a large fraction of its injected energy within radii less than

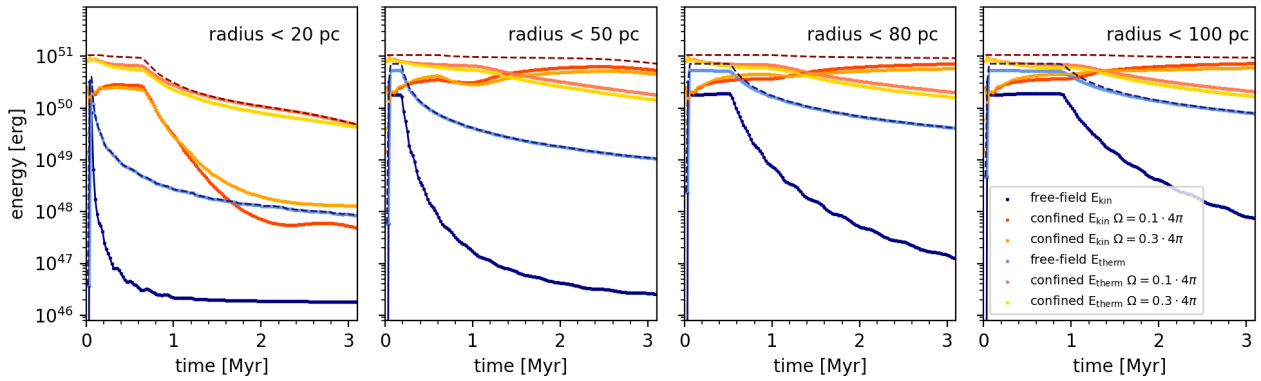


Figure 9. Kinetic and thermal energy contained within a radius of 20 pc, 50 pc, 80 pc and 100 pc from the progenitor in the simulation adiabatic runs. The free-field kinetic energy curve is plotted in dark blue and thermal in light blue. The semi-confined (solid angle of $\Omega = 0.1 \times 4\pi$) kinetic energy is in red and thermal in pink. For the run with a larger channel (solid angle of $\Omega = 0.3 \times 4\pi$), its kinetic energy is given by the orange curve and thermal is in yellow. The total energies of free-field and semi-confined (solid angle of $\Omega = 0.1 \times 4\pi$) are plotted in dashed dark blue and dark red lines respectively.

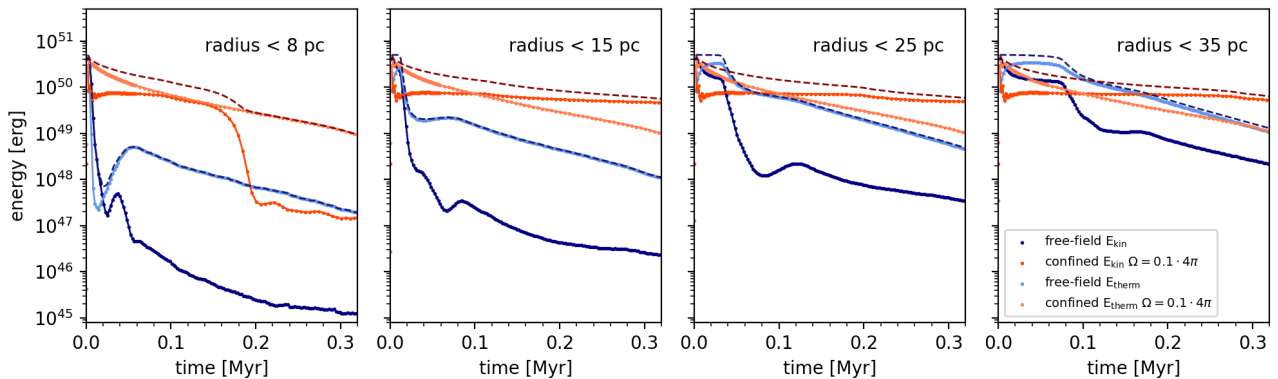


Figure 10. Kinetic and thermal energy contained within a radius of 8 pc, 15 pc, 25 pc and 35 pc from the progenitor in the cooling runs. The dark blue and light blue curves are the kinetic and thermal energy in the free-field case. The semi-confined kinetic energy is in dark orange and thermal is in light orange. We show only the runs with channel size $\Omega = 0.1 \times 4\pi$. The total energies of free-field and semi-confined are plotted in dashed dark blue and dark red lines.

50 pc, as opposed to the free-field case where energy is rapidly lost to beyond 100 pc. Similar to the multiple-channel tests, we again find that having a slightly larger opening does not lead to any significant changes in the SN output.

As with before, we look at the case with radiative losses incorporated. Fig. 10 shows the kinetic and thermal energy contained within 8 pc, 15 pc, 25 pc and 35 pc. The internal energy drops in both cases from the cooling, however, the kinetic energy in the semi-confined SN is almost fully retained within 8–15 pc throughout the remnant’s evolution. This is much greater than the amount of kinetic energy retained in the free-field case. The bump seen at around 0.1 Myr in the free-field curve is likely caused by a reverse shock. From Fig. 9 and 10, we can conclude that semi-confined SN can significantly increase the kinetic energy deposition at smaller distances from the progenitors. Hence, the dynamical impact of the outflow may be greater than those predicted from 1-D models (see also e.g. Gendelev & Krumholz 2012).

These results also supplement to the findings of Rosen et al. (2014), who suggested that the large fraction of missing energy within feedback-driven bubbles is attributed to the presence of holes on the porous shell. The authors showed that the shell cover fraction C_f should be around the range 0.36–0.95 in order to explain their observed luminosities. Similarly, Dale et al. (2014) found that the leakage factor lie mostly at around 0.6–0.8, though both studies only

accounted for pre-SN feedback. Our findings here suggest that C_f may need to be lower than at least 0.7, which otherwise the confinement effect would still dominate and prevent the bubble from losing the required amount of energy.

4.5 Turbulence driving

We showed in the previous section that semi-confined SNe are capable of sustaining a higher level of kinetic input at short distances to its progenitor compared to spherical expansions. Since SNe are one of the primary drivers of turbulence in the ISM (e.g. Elmegreen & Scalo 2004; Balsara et al. 2004; MacLow 2004; Bacchini et al. 2020), we further investigate the semi-confined SNe’s mechanical input by assessing their ability to induce compressive and solenoidal turbulent motions.

In fact, shocks expanding into a low-density circumstellar medium naturally produces helicity in the ISM. When the shell of SN ejecta decelerates after interacting with the shocked ambient gas, the ejecta materials at the interface become unstable to Rayleigh-Taylor instability and subsequently develop the so-called Rayleigh-Taylor fingers that protrude into the surrounding medium (Jun et al. 1996; Blondin & Ellison 2001). As the fingers grow, the shear at the contact boundaries gives rise to secondary Kelvin-Helmholtz instability, generating vorticities along the fingers (e.g. Bucciantini, N. et al. 2004). Such

eddies might in turn enhance the growth of the fingers by supplying extra rotational kinetic energy (Jun et al. 1996). Even in the absence of hydrodynamic instabilities, strong shocks that interact with a clumpy turbulent medium also naturally generate velocity dispersions (Dobbs & Bonnell 2008; Bonnell et al. 2013) and helicity fluctuations in the post-shock regions (Balsara et al. 2001; Balsara et al. 2004). A similar finding has been reported in Padoan et al. (2016), that the solenoidal component in the turbulence must be greater than the compressive if SN interacts with a medium whose density gradients are in random directions.

Though turbulence is not being added in our simulations as a starting condition, our semi-confined SN model ubiquitously involves shock collisions with cavity walls. We thus expect a larger amount of shear and vortices to develop in the outflows compared to free-fields (see the plumes shown in Fig. 2). As the fluid moves through the channels, it may be also subjected to Kelvin-Helmholtz instability that generates small-scale eddies. A higher helicity in the flow implies a stronger solenoidal component in its velocity field. Solenoidal turbulences are known for their ability to support against gravitational collapse and regulate star formation (e.g. Rani et al. 2022).

To compare the amount of vorticity in the semi-confined and the free-field cases, we decompose their velocities to plot the kinetic energy spectra. Our method works by, first, imposing a cubical Cartesian grid onto the simulation that is centred at the progenitor and covers a large fraction of the envelope’s volume. The grid vertices serve as interpolation points where we obtain the fluid’s velocity from the neighbouring particles. The length of the grid and the spacing between the vertices hence define our resolution limits. The velocity field is subsequently passed into a Helmholtz-Hodge decomposition algorithm to separate the total velocity into solenoidal (divergence-free) and compressive (curl-free) components. The velocity cubes for each component are then passed into a fast Fourier transform algorithm to produce their kinetic energy spectra in wave number space. We also emphasize that, since we are interested only in the generation of local kinetic motions in the post-shock regions, the grid does not necessarily cover the shock front.

Fig. 11 shows the spectra extracted from the adiabatic runs. The grid has 300^3 interpolation points with a length of 100 pc (radius of 50 pc from the progenitor). We compare semi-confined to free-field at time instances where their shock fronts are at similar distances from the progenitor, hence a similar driving scale. The resolution limits constrained by the grid spacing and its full length are greyed out to indicate the parts of the curve to be neglected. We compare their spectra at shock front radii of 40 pc, 100 pc and 140 pc respectively. The semi-confined curves are plotted in solid lines and those of free-field are in dashed lines, each with their total kinetic energy and their solenoidal and compressive components displayed. The peaks seen at large length scales indicate a strong driving. Note however that the location of this peak is likely limited by the length of our grid, hence we consider here only their intensities rather than their precise wave numbers.

As seen from the first panel in Fig. 11, the free-field SN rapidly reaches a distance of 40 pc shortly after detonation, creating a very prominent peak at the longer length-scales that indicates strong driving. Once the shock front exits the grid and reaches 100 pc (second panel), the peak falls back to a similar level as the semi-confined case. At this point, their kinetic energy spectra are alike, though the solenoidal component in the free-field case is significantly weaker due to the lack of collisions, which in turn prevents eddies from forming. The spectra remained steady until the shock fronts reach 140 pc (third panel), and thereafter the free-field kinetic energies begin to

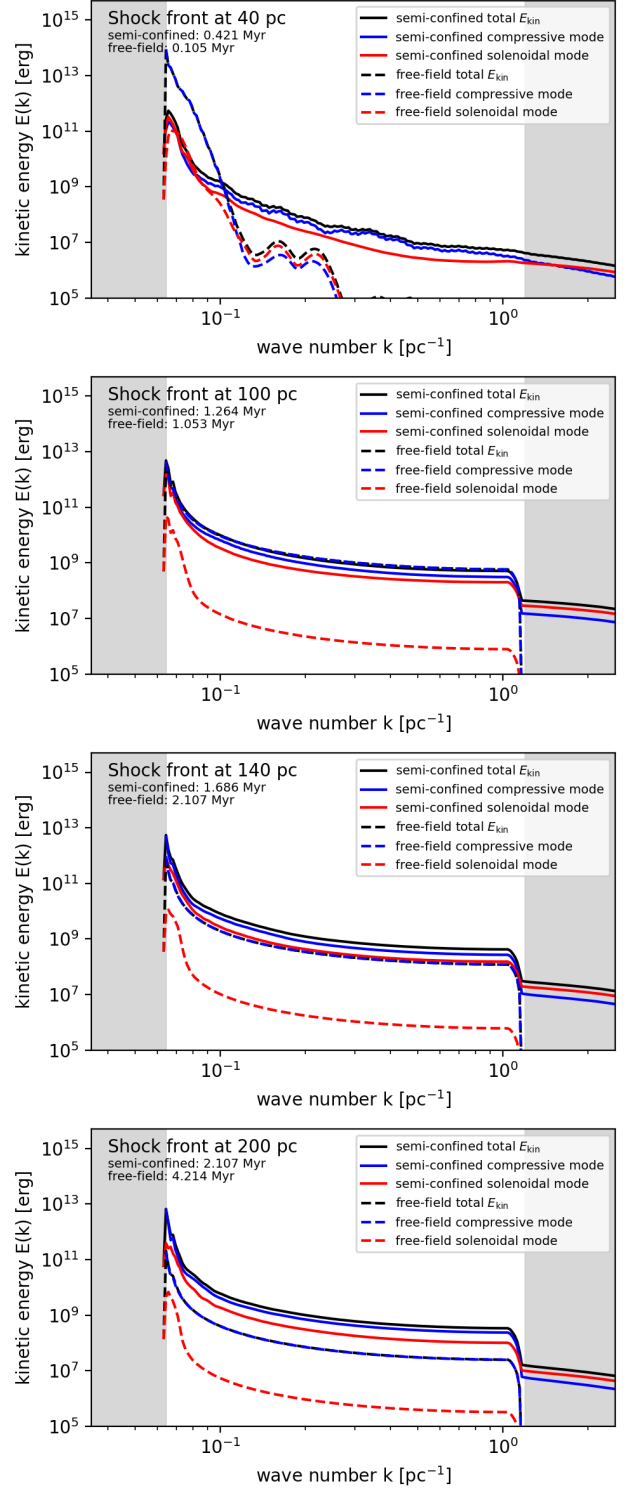


Figure 11. Kinetic energy spectra of the adiabatic runs comparing semi-confined (solid line) to free-field (dashed line) at times where their shock fronts both reach a distance of approximately 40 pc, 100 pc, 140 pc and 200 pc from the progenitor. The total kinetic energy is plotted in black; its solenoidal and compressive components are in red and blue respectively. Note the time difference between the free-field and the semi-confined curve being compared in each panel. The greyed-out regions indicate the resolution limits and may be disregarded.

decline. By the time the shocks reach a distance of 200 pc (fourth panel), the local kinetic energies in the free-field become much lower, particularly in its solenoidal components. To the contrary, the semi-confined SN maintained its spectra intensities even when its shock front has reached such large distances. This result is in line with our findings from Fig. 5, that semi-confined progenitors can create more sustained perturbations to its local environment.

For the simulations with radiative cooling, we use a smaller grid of 200^3 vertices with a total length of 60 pc (radius of 30 pc from the progenitor). The spectra are shown in Fig. 12 and the grey areas mark the resolution limits. We compare the semi-confined to the free-field case where their shock fronts have reached distances of 15 pc, 30 pc, 40 pc and 50 pc. The kinetic energies of the semi-confined are higher during the initial times at the shorter length-scales when the energy is *just* driven out the channel by the hot over-pressured cavity. This is likely due to the plumes that form in the outflows as it interacts with the warm envelope gas. However, when the shock fronts reach distances of around 40 pc, the compressive component of the free-field kinetic energy becomes higher than that of semi-confined (see third and fourth panel).

This seems to be at odds with our findings in Fig. 10. The semi-confined SN should have retained a larger amount of kinetic energy within 15 pc from the progenitor (see second panel) and up to at least 35 pc (see fourth panel), which covers the full length of our grid. An explanation to this discrepancy is that the outflows from semi-confined had the majority of its kinetic energy stored in the eddies developed from the plumes, whose spatial length-scales were too small to be captured by the grid used for generating the spectra in Fig. 12. It is no surprise that cooling would give rise to fluid instabilities and introduce higher level of vorticity in the outflows as it reduces the gas thermal pressure. This may be analogous to the idea discussed in Kuiper et al. (2012), that radiation-driven cavities around young massive stars are prone to Rayleigh-Taylor instabilities when the radiative pressure support is underestimated.

To show that this is indeed the case, we use a higher resolution grid with smaller spacings – 200^3 vertices and a full length of 15 pc. This grid is not centred at the origin but at +25 pc on the x-axis, such that the grid volume covers the post-shock region and is not entirely occupied by the molecular cloud. We compare the kinetic energy spectra of the semi-confined and the free-field simulation when their shock fronts reach 45 pc away from the progenitor. Fig. 13 shows the result. As hypothesized, at smaller length-scales, the kinetic energy of the semi-confined case is now greater than the free-field. The compressive component of the free-field is also an order of magnitude lower. We conclude from these results that semi-confined SNe are more capable of sustaining solenoidal turbulence at the *smaller* length-scales, owing to the vorticities generated by the plumes in the outflow.

5 DISCUSSIONS AND SUMMARY

In this paper, we presented a theoretical model of a SN explosion that is partially confined within a bubble, or cavity, carved by its earlier stellar feedback. As past studies revealed that SN energy often leave their natal cloud preferentially through low-density channels, we investigated how the SN output in this scenario would differ to that from a typical 1-D blast model. We showed that our analytical model successfully predicts the outflow velocities from 3-D numerical simulations, even for cases with radiative cooling and with multiple channels around the porous cavity shell. We also studied the gas properties of the outflow, its energy deposition, and the driven turbu-

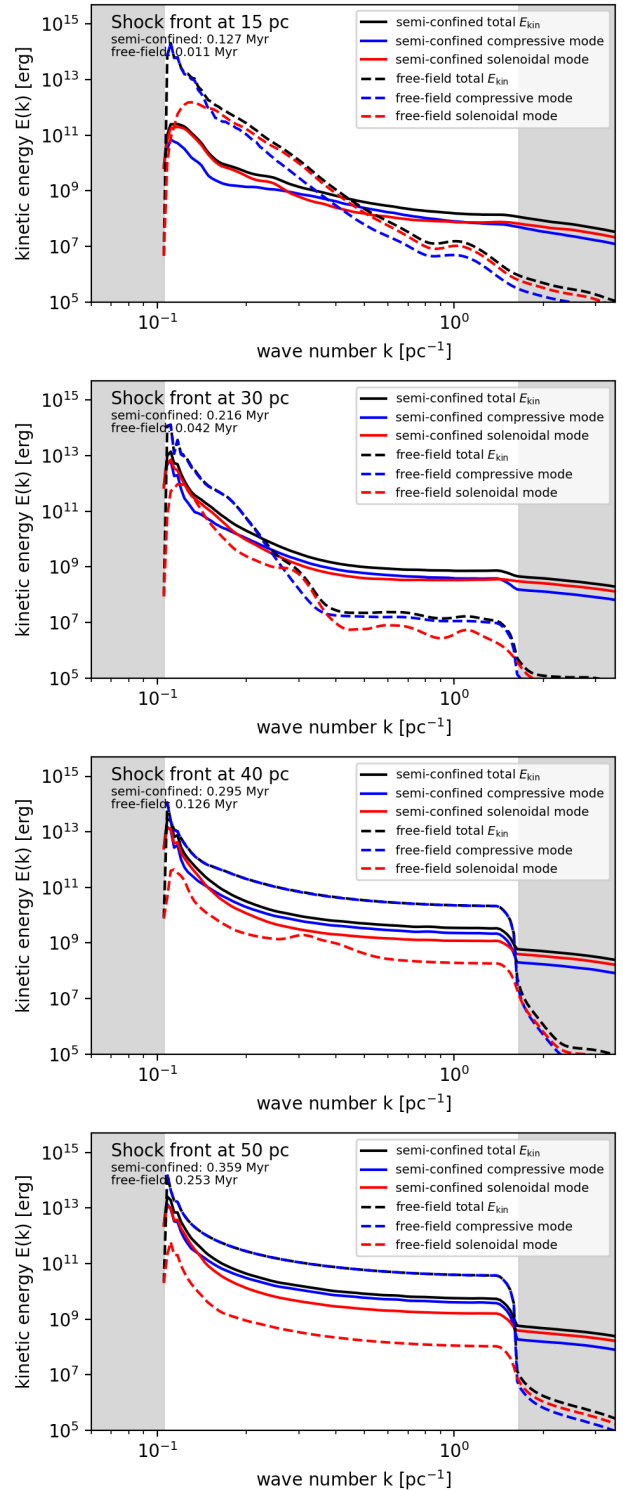


Figure 12. Same as Fig. 11 but for the cooling runs. Because of the shorter time- and length-scales, the spectra are compared at times when their shock fronts reach distances of approximately 15 pc, 30 pc, 40 pc and 50 pc. Greyed-out regions mark the resolution limits.

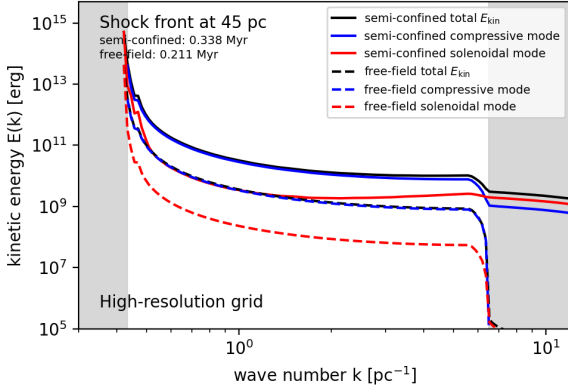


Figure 13. Kinetic energy spectrum of semi-confined (solid line) and free-field SN (dashed line) in the cooling run at times where their shock fronts are at 45 pc, generated with a small but higher resolution grid to capture the eddies on shorter length-scales. Greyed-out regions mark the resolution limits.

lence. Our results showed that semi-confined SNe impose stronger dynamical impact on the small scales, as they deposit a larger amount of kinetic energy at radii closer to the progenitor. The timescale of the coupling are extended thanks to the slow pressure relief process inside the cavity. From the kinetic energy spectra, the solenoidal turbulence driven by semi-confined SN is also amplified at smaller length-scales via the development of plumes.

A few interpretations can be drawn from these results:

(i) Large-scale simulations that rely on Sedov-Taylor-like solutions as sub-grid models of SN might overestimate the impact radius and underestimate the amount of local kinetic energy deposition.

(ii) That semi-confined SNe drive stronger solenoidal turbulence at smaller scales may indicate a higher ability to regulate star formation in their local environments.

(iii) An extended kinetic energy coupling timescale with its natal molecular cloud can imply that a lower SN rate may be sufficient to reproduce the observed local star formation efficiencies.

(iv) Peculiar velocity profiles observed around highly asymmetrical SN remnants can be explained by outflows through gaps on the shell, whose velocities can be much higher than if the SN shock is expanding isotopically.

(v) Outflows from small holes on porous shells may be treated as individual streamlines. It provides good estimates of the outflow velocities and pressure from the bubble just using simple fluid equations that govern adiabatic incompressible flows.

(vi) In order to explain the energy or pressure loss from feedback-driven bubbles (e.g. [Rosen et al. 2014](#); [Lopez et al. 2014](#)), the cover fraction of the shell must be sufficiently small. We showed in our simulations that even a total opening area of 40% of the spherical shell surface does not lead to significant pressure loss from the cavity (cf. [Fig. 8](#)), provided that the gas is leaving through small channels with solid angles less than $0.3 \times 4\pi$ [Sr]. We suggest that it is important to distinguish whether the cover fraction refers to a big hole on the shell or multiple small gaps.

(vii) Since shock-induced gravitational collapse often require the shocks to be of sufficiently low velocity to create mild compression (e.g. [Boss 1995](#); [Kinoshita et al. 2021](#)), a higher dynamical input from SN might imply a lower chance of locally triggering star formation.

The differences between a semi-confined model and a spherically symmetric model have plenty of implications on the large-scale evo-

lutions. We argue that it is necessary to account for the confinement effects and the collimated outflows from SNe in the 1-D sub-grid models. This may be done via parametrization accompanied with statistical techniques. Additionally, since most of the current SN models can already account for the non-uniformity of the ambient ISM, incorporating density fluctuations into our models' background medium before carrying out the comparisons may provide more useful information on the limitations of these 1-D models. Nevertheless, a major shortcoming of our study is the overly solid cavity wall, which was created only to replicate the analytical model. Turbulent mixing at the interface between SN remnant and the shell could have a significant impact on the energy dissipation (e.g. [Mackey et al. 2015](#)). As such, testing our findings in more realistic turbulent molecular cloud environments should be the next step to verify our findings.

On a final note, it may be beneficial to extend this study by incorporating magnetic fields. Spherical shells driven by expanding HII regions that collide with ISM materials are capable of compressing magnetic fields and bending the field lines along the dense shells (e.g. [Pattle et al. 2023](#); [Tahani et al. 2023](#)). These tangential fields might suppress shell fragmentation and resist the formation of radiation-driven pillars or protrusions from the HII regions ([Hennebelle & Inutsuka 2019](#)). It may be of interest to study whether or not magnetic fields can hinder SN outflows from leaky feedback bubbles.

ACKNOWLEDGEMENTS

CSCL thank Ben Keller and Craig Yanitski for their very helpful suggestions on the project idea. CSCL also thank Daniel Seifried and colleagues from Theoretical Astrophysics group Cologne for their comments and advices regarding this work. This project was supported by the STFC training grant ST/W507817/1 (Project reference 2599314). The simulations were performed using the HPC Kennedy, operated by University of St Andrews. The SPH figures in this paper were created using the python package SARRACEN ([Harris & Tricco 2023](#)). The Helmholtz-Hodge decomposition algorithm was developed based on the python code HELMHOLTZ ([Shi 2018](#)). The algorithm for generating kinetic energy spectra was developed based on the python code TKESPEC ([Saad 2014](#)).

DATA AVAILABILITY

The data associated with this paper, including the simulations codes and outputs, can be made available upon reasonable request to the corresponding author.

REFERENCES

- Aschenbach B., Leahy D. A., 1999, *A&A*, 341, 602
 Bacchini C., Fraternali F., Iorio G., Pezzulli G., Marasco A., Nipoti C., 2020, *A&A*, 641, A70
 Balsara D., Benjamin R. A., Cox D. P., 2001, *ApJ*, 563, 800
 Balsara D. S., Kim J., Mac Low M.-M., Mathews G. J., 2004, *ApJ*, 617, 339
 Bisbas T. G., et al., 2015, *MNRAS*, 453, 1324
 Blondin J. M., Ellison D. C., 2001, *ApJ*, 560, 244
 Bonnell I. A., Dobbs C. L., Smith R. J., 2013, *MNRAS*, 430, 1790
 Borkowski K., Szymkowiak A. E., Blondin J. M., Sarazin C. L., 1996, *ApJ*, 466, 866
 Borkowski K. J., Gwynne P., Reynolds S. P., Green D. A., Hwang U., Petre R., Willett R., 2017, *ApJL*, 837, L7
 Boss A. P., 1995, *ApJ*, 439, 224

- Bucciantini, N., Amato, E., Bandiera, R., Blondin, J. M., Del Zanna, L., 2004, *A&A*, 423, 253
- Castor J., McCray R., Weaver R., 1975, *ApJ*, 200, L107
- Chevalier R. A., Liang E. P., 1989, *ApJ*, 344, 332
- Chow E., Monaghan J., 1997, *J. Comput. Phys.*, 134, 296
- Cowie L. L., McKee C. F., Ostriker J. P., 1981, *ApJ*, 247, 908
- Creasey P., Theuns T., Bower R. G., Lacey C. G., 2011, *MNRAS*, 415, 3706
- Dale J. E., Bonnell I. A., 2008, *MNRAS*, 391, 2
- Dale J. E., Ercolano B., Bonnell I. A., 2012, *MNRAS*, 424, 377
- Dale J. E., Ngoumou J., Ercolano B., Bonnell I. A., 2013, *MNRAS*, 436, 3430
- Dale J. E., Ngoumou J., Ercolano B., Bonnell I. A., 2014, *MNRAS*, 442, 694
- Dalgarno A., McCray R. A., 1972, *Annu. Rev. Astron. Astrophys.*, 10, 375
- Dalla Vecchia C., Schaye J., 2012, *MNRAS*, 426, 140
- Dobbs C. L., Bonnell I. A., 2008, *MNRAS*, 385, 1893
- Draine B. T., 2011, *ApJ*, 732, 100
- Dwarkadas V. V., 2005, *ApJ*, 630, 892
- Dwarkadas V. V., 2007, *Astrophys Space Sci*, 307, 153–158
- Díaz J., Rigby S., 2022, *Shock Waves*, 32, 405–415
- Elmegreen B. G., Scalo J., 2004, *ARA&A*, 42, 211
- Falle S. A. E. G., Garlick A. R., 1982, *MNRAS*, 201, 635
- Fang J., Yu H., Zhang L., 2016, *MNRAS*, 464, 940
- Feldgun V., Karinski Y., Yankelevsky D., 2011, *Int. J. Impact Eng.*, 38, 964
- Feldgun V., Karinski Y., Edri I., Yankelevsky D., 2016, *Int. J. Impact Eng.*, 90, 46
- Fichtner Y. A., Grassitelli L., Romano-Díaz E., Porciani C., 2022, *MNRAS*, 512, 4573
- Fichtner Y. A., Mackey J., Grassitelli L., Romano-Díaz E., Porciani C., 2024, *A&A*, 690, A72
- Freyer T., Hensler G., Yorke H. W., 2006, *ApJ*, 638, 262
- Geen S., de Koter A., 2022, *MNRAS*, 509, 4498
- Geen S., Bieri R., de Koter A., Kimm T., Rosdahl J., 2023, *MNRAS*, 526, 1832
- Gendeleev L., Krumholz M. R., 2012, *ApJ*, 745, 158
- Gingold R. A., Monaghan J. J., 1977, *MNRAS*, 181, 375
- Goswami S., et al., 2021, *A&A*, 650, A203
- Haid S., Walch S., Naab T., Seifried D., Mackey J., Gatto A., 2016, *MNRAS*, 460, 2962
- Haid S., Walch S., Seifried D., Wunsch R., Dinnbier F., Naab T., 2018, *MNRAS*, 478, 4799
- Harper-Clark E., Murray N., 2009, *AAS*, 693, 1696
- Harris A., Tricco T. S., 2023, *JOSS*, 8, 5263
- Hennebelle P., Iffrig O., 2014, *A&A*, 570, A81
- Hennebelle P., Inutsuka S.-i., 2019, *Front. Astron. Space Sci.*, 6
- Hopkins P. F., Quataert E., Murray N., 2011, *MNRAS*, 417, 950
- Hosokawa T., Inutsuka S.-i., 2006, *ApJ*, 646, 240
- Hugoniot H., 1887, *J. de l'Ecole Polytechnique*, 57
- Joung M. K. R., Mac Low M.-M., 2006, *ApJ*, 653, 1266
- Jun B.-I., Jones T. W., Norman M. L., 1996, *ApJ*, 468, L59
- Katz N., 1992, *ApJ*, 391, 502
- Keller B. W., Kruijssen J. M. D., 2022, *MNRAS*, 512, 199
- Keller B. W., Wadsley J., Benincasa S. M., Couchman H. M. P., 2014, *MNRAS*, 442, 3013
- Keller B. W., Wadsley J., Couchman H. M. P., 2015, *MNRAS*, 453, 3499
- Kim C.-G., Ostriker E. C., Raileanu R., 2016, *ApJ*, 834, 25
- Kinoshita S. W., Nakamura F., Wu B., 2021, *ApJ*, 921, 150
- Koyama H., Inutsuka S.-i., 2002, *ApJ*, 564, L97
- Krumholz M. R., Klein R. I., McKee C. F., Offner S. S. R., Cunningham A. J., 2009, *Science*, 323, 754–757
- Kuiper R., Klahr H., Beuther H., Henning T., 2012, *A&A*, 537, A122
- Kumar M. S. N., 2013, *A&A*, 558, A119
- Körtgen B., Seifried D., Banerjee R., Vázquez-Semadeni E., Zamora-Avilés M., 2016, *MNRAS*, 459, 3460
- Larson R. B., 1974, *MNRAS*, 169, 229
- Lau C. S. C., Petkova M. A., Bonnell I. A., 2024, preprint, (arXiv:2410.15227)
- Lopez L. A., Krumholz M. R., Bolatto A. D., Prochaska J. X., Ramirez-Ruiz E., 2011, *ApJ*, 731, 91
- Lopez L. A., Krumholz M. R., Bolatto A. D., Prochaska J. X., Ramirez-Ruiz E., Castro D., 2014, *ApJ*, 795, 121
- Lucas W. E., Bonnell I. A., Forgan D. H., 2017, *MNRAS*, 466, 5011
- Lucas W. E., Bonnell I. A., Dale J. E., 2020, *MNRAS*, 493, 4700
- Lucy L. B., 1977, *AJ*, 82, 1013
- Mac Low M.-M., Klessen R. S., 2004, *Rev. Mod. Phys.*, 76, 125
- MacLow M.-M., 2004, *Ap&SS*, 289, 323–331
- Mackey J., Mohamed S. S., Gvaramadze V. V., Kotak R., Langer N., Meyer D. M.-A., Moriya T. J., Neilson H. R., 2014, *Nature*, 512, 282
- Mackey J., Gvaramadze V. V., Mohamed S., Langer N., 2015, *A&A*, 573, A10
- McKee C. F., Ostriker J. P., 1977, *ApJ*, 218, 148
- Meyer D. M. A., 2024, *MNRAS*, 530, 539
- Meyer D. M.-A., Langer N., Mackey J., Velázquez P. F., Gusdorf A., 2015, *MNRAS*, 450, 3080
- Minière J., Bouquet S. E., Michaut C., Sanz J., Mancini M., 2018, *A&A*, 617, A133
- Morfill G. E., Tenorio-Tagle G., 1983, *Space Sci. Rev.*, 36, 93
- Oey M. S., Clarke C. J., 1997, *MNRAS*, 289, 570
- Oku Y., Tomida K., Nagamine K., Shimizu I., Cen R., 2022, *ApJSS*, 262, 9
- Osterbrock D. E., 1974, *Astrophysics of gaseous nebulae*. W. H. Freeman and Company
- Ostriker J. P., McKee C. F., 1988, *Rev. Mod. Phys.*, 60, 1
- Ostriker E. C., Shetty R., 2011, *ApJ*, 731, 41
- Padoan P., Pan L., Haugbølle T., Nordlund Å., 2016, *ApJ*, 822, 11
- Pattle K., Fissel L., Tahani M., Liu T., Ntormousi E., 2023, in *Protostars and Planets VII*. p. 193
- Petkova M. A., Laibe G., Bonnell I. A., 2018, *J. Comput. Phys.*, 353, 300
- Petkova M. A., Vandenbroucke B., Bonnell I. A., Kruijssen J. M. D., 2021, *MNRAS*, 507, 858
- Pfrommer C., Pakmor R., Simpson C. M., Springel V., 2017, *ApJ*, 847, L13
- Price D. J., 2008, *J. Comput. Phys.*, 227, 10040
- Price D. J., et al., 2018, *PASA*, 35, e031
- Raga A. C., Cantó J., Rodríguez L. F., 2012, *MNRAS*, 419, L39
- Rahner D., Pellegrini E. W., Glover S. C. O., Klessen R. S., 2017, *MNRAS*, 470, 4453
- Rahner D., Pellegrini E. W., Glover S. C. O., Klessen R. S., 2018, *MNRAS*, 483, 2547
- Rani R., Moore T. J. T., Eden D. J., Rigby A. J., 2022, *MNRAS*, 515, 271
- Rankine W. J. M., 1870, *Phil. Trans. R. Soc.*, 160, 277–288
- Rogers H., Pittard J. M., 2014, *MNRAS*, 441, 964
- Romano L. E. C., Behrendt M., Burkert A., 2024, *A&A*, 965, 168
- Rosdahl J., Schaye J., Dubois Y., Kimm T., Teyssier R., 2017, *MNRAS*, 466, 11
- Rosen A. L., Lopez L. A., Krumholz M. R., Ramirez-Ruiz E., 2014, *MNRAS*, 442, 2701
- Saad T., 2014, *tkspec*, <https://turbulence.utah.edu/code/>
- Schoenberg I. J., 1946, *Quart. Appl. Math.*, 4, 45
- Sedov L. I., 1946, *Appl. Math. Mech.*, 10, 241
- Shi X., 2018, Helmholtz-Hodge decomposition using fft, <https://github.com/shixun22/helmholtz/blob/master/helmholtz.py>
- Spitzer L., 1978, *Physical processes in the interstellar medium*. Wiley
- Springel V., Hernquist L., 2002, *MNRAS*, 333, 649
- Stinson G., Seth A., Katz N., Wadsley J., Governato F., Quinn T., 2006, *MNRAS*, 373, 1074
- Strömgren B., 1939, *ApJ*, 89, 526
- Sutherland R. S., Dopita M. A., 1993, *ApJS*, 88, 253
- Tahani M., et al., 2023, *ApJ*, 944, 139
- Taylor G. I., 1950, *Proc. R. Soc. Lond. A*, 201, 159–174
- Tenorio-Tagle G., Bodenheimer P., Yorke H. W., 1985, *A&A*, 145, 70
- Thacker R. J., Couchman H. M. P., 2000, *ApJ*, 545, 728
- Uchida H., Tsunemi H., Katsuda S., Kimura M., 2008, *ApJ*, 688, 1102
- Vandenbroucke B., Camps P., 2020, *A&A*, 89, 614
- Vandenbroucke B., Wood K., 2018, *Astron. Comput.*, 23, 40
- Vázquez-Semadeni E., Gomez G. C., Jappsen A. K., Ballesteros-Paredes J., Gonzalez R. F., Klessen R. S., 2007, *ApJ*, 657, 870
- Voronoi G., 1908, *Journal für die reine und angewandte Mathematik*, 1908, 198

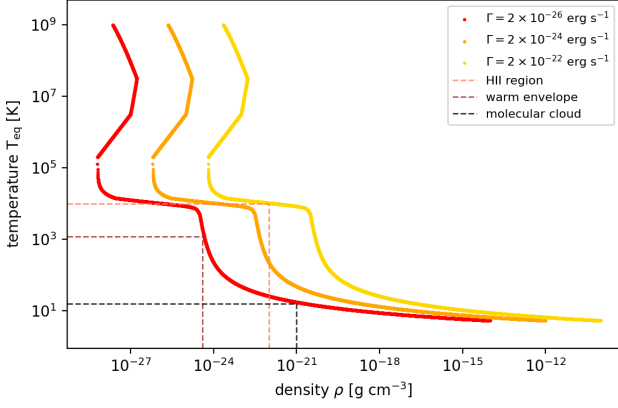


Figure A1. Equilibrium temperatures T_{eq} as a function of gas local density ρ obtained by solving the thermal equilibrium equation, $n_H \Gamma - n_H^2 \Lambda(T) = 0$, where $\Lambda(T)$ is defined by a cooling curve, and heating term is $\Gamma = 2 \times 10^{-26} \text{ erg s}^{-1}$ (red), $\Gamma = 2 \times 10^{-24} \text{ erg s}^{-1}$ (orange) and $\Gamma = 2 \times 10^{-22} \text{ erg s}^{-1}$ (yellow). The red curve shows equilibrium temperatures when the gas is only subjected to background FUV heating, and yellow curves shows the equilibrium temperatures under stellar photoionization heating. Dashed lines mark the temperatures of the cloud (black), the envelope (brown) and the HII region (light brown), whose densities are given in Section 4.1.1.

- Walch S., Naab T., 2015, MNRAS, 451, 2757
 Walch S. K., Whitworth A. P., Bisbas T., Wünsch R., Hubber D., 2012, MNRAS, 427, 625
 Wannier P. G., Lichten S. M., Morris M., 1983, ApJ, 268, 727
 Wareing C. J., Pittard J. M., Falle S. A. E. G., 2016, MNRAS, 465, 2757
 Wareing C. J., Pittard J. M., Falle S. A. E. G., 2017, MNRAS, 470, 2283
 Weaver R., McCray R., Castor J., Shapiro P., Moore R., 1977, ApJ, 218, 377
 Whitworth A. P., Bhattal A. S., Chapman S. J., Disney M. J., Turner J. A., 1994, Astron.Astrophys., 290, 421
 Wolfire M. G., Hollenbach D., McKee C. F., Tielens A. G. G. M., Bakes E. L. O., 1995, ApJ, 443, 152
 Wolfire M. G., Hollenbach D., McKee C. F., 2010, ApJ, 716, 1191

APPENDIX A: EQUILIBRIUM TEMPERATURES

To efficiently update the internal energies with the implicit method (equation 33), we pre-compute and tabulate the equilibrium temperatures for a range of particle densities ρ , then interpolate from this table during runtime. Fig. A1 plots the solution temperatures T_{eq} that satisfy the thermal equilibrium equation $n_H \Gamma - n_H^2 \Lambda(T) = 0$, where the background heating is $\Gamma = 2 \times 10^{-26} \text{ erg s}^{-1}$ (red) (Koyama & Inutsuka 2002) and the cooling $\Lambda(T)$ is governed by the cooling curve from Joungh & Mac Low (2006, Fig. 1). Note that $n_H = \rho/m_H$. The high-density regime in Fig. A1 is akin to the equilibrium temperature plot in e.g. Bonnell et al. (2013, Fig. 2). The low-density regime, however, is multi-valued, meaning there can be more than one thermal equilibrium at certain gas densities. The method to identify the equilibrium to which the particle should approach is detailed in Lau et al. (2024).

We also plot in Fig. A1 the solutions for $\Gamma = 2 \times 10^{-24} \text{ erg s}^{-1}$ (orange) and $\Gamma = 2 \times 10^{-22} \text{ erg s}^{-1}$ (yellow) to illustrate the effect of increased heating. The latter is roughly equal to the stellar photoionization heating rate for cloud densities of around $10^{-21} \text{ g cm}^{-3}$ (cf. Lau et al. 2024, Fig. 9). Hence, the yellow curve governs the equilibrium temperatures within the HII regions. For $\rho_{\text{HII}} = 10^{-22} \text{ g cm}^{-3}$, its temperatures is at around 10^4 K (dashed light brown). Elsewhere

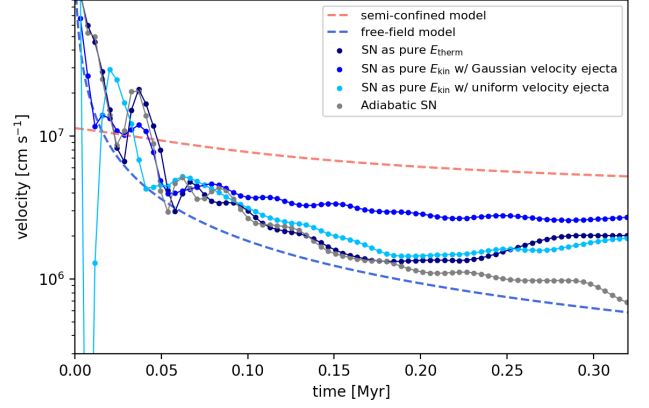


Figure B1. Time-evolution of gas velocity at the detector location in the cooling run for a free-field SN that is injected as pure thermal energy (navy), one that is injected as pure kinetic energy with uniform radial velocities assigned to the ejecta particles (light blue), and one that is also injected as pure kinetic energy but with ejecta radial velocities distributed in the form of a skewed Gaussian function (dark blue; identical to the free-field curve in Fig. 6 first panel). Result from an adiabatic run is plotted for comparison (grey). The analytical solutions of free-field and semi-confined are shown in blue and red dashed lines respectively.

in the simulation, the gas temperatures follow the red curve. Thus, the cloud with density $\rho_{\text{cloud}} = 10^{-21} \text{ g cm}^{-3}$ is at 10 K (dashed black), and the warm envelope with $\rho_{\text{env}} = 4 \times 10^{-25} \text{ g cm}^{-3}$ is at 10^3 K (dashed brown).

APPENDIX B: FREE-FIELD OUTFLOW GAS VELOCITY AT DETECTOR IN COOLING RUNS

We discuss the reasons as to why the free-field velocities at the detector in the cooling run remain steady throughout its evolution (see Fig. 6; first panel). Such discrepancy with the analytical model may be explained using several extra test simulations. The results are presented in Fig. B1. The dark blue curve is identical to that in Fig. 6.

First, by simply switching off cooling (grey), we recover the analytical solution. Despite the SN is injected as pure kinetic energy, the energy is soon thermalized in the shocks and thus reproduces the adiabatic curve with SN injected as thermal energy, shown in Fig. 5. This indicates that the peculiar velocity curve in Fig. 6 is a direct consequence of our cooling implementation.

Once radiative cooling effects are incorporated, velocities from a SN injected as pure thermal energy (navy) remain similar to the adiabatic case only up to around 0.18 Myr – beyond this point, the curve begins to rise. The reason may be attributed to the low gas density in our free-field ambient medium. Fig. A1 shows that gas equilibrium temperatures T_{eq} at densities beneath $10^{-25} \text{ g cm}^{-3}$ rise up to 10^4 K , which corresponds to the ISM warm phase, from the fact that cooling is highly inefficient in low-density regions. The gas around the evacuated progenitor drops in density and in turn becomes heated by the background heating constant Γ (cf. Koyama & Inutsuka 2002). As thermal energy drives gas expansions, this heating causes the rise in velocities towards the later stages.

The second factor that was responsible for the large velocities at the early stages in Fig. 6 (dark blue in Fig. B1) is the velocity profile of the ejecta particles. In our simulations, we set the radial velocities to take the form of a skewed Gaussian function in order to create a dense shell. However, doing so extends the driving timescale and

creates a *series* of shock waves, deviating it from being an energy point source as assumed in the Sedov-Taylor solution. We illustrate our point by performing an identical test run but with a uniform velocity profile assigned to the ejecta particles (light blue). It can be seen that setting up a coherent shock immediately recovers the pure thermal energy case (navy), in which the SN is closest to being a point source explosion. The curves agree well with the analytical model before they are ‘deflected’ by the heating.

From the above, we argue that the flat velocity curve in Fig. 6 is only a consequence of our low-density ambient medium and our choice of ejecta velocity distribution. Despite these influences, however, the perturbations induced by a free-field SN are still below that of the semi-confined. It hence provides strong evidence to support the idea that semi-confined SNe can impose a higher dynamical impact locally.

This paper has been typeset from a $\text{\TeX}/\text{\LaTeX}$ file prepared by the author.